The Samapleu mafic-ultramafic intrusion (Western Ivory Coast): Cumulate of a High-Mg Basaltic Magma with (coeval) ultra-high temperature - medium pressure metamorphism

Franck Gouedji, Christian Picard, Marc-Antoine Audet, Philippe Goncalves, Yacouba Coulibaly, Bouaké Bakayoko

Accepted Manuscript

Geological Society, London, Special Publications

The Samapleu mafic-ultramafic intrusion (Western Ivory Coast): Cumulate of a High-Mg Basaltic Magma with (coeval) ultra-high temperature - medium pressure metamorphism

Franck Gouedji, Christian Picard, Marc-Antoine Audet, Philippe Goncalvés, Yacouba Coulibaly & Bouaké Bakayoko

DOI: https://doi.org/10.1144/SP502-2019-130

Received 31 July 2019
Revised 20 March 2020
Accepted 24 March 2020

The Samapleu mafic-ultramafic intrusion (Western Ivory Coast): Cumulate of a High-Mg Basaltic Magma with (coeval) ultra-high temperature - medium pressure metamorphism

Franck GOUEDJI[a*], Christian PICARD[d], Marc-Antoine AUDET[b], Philippe GONCALVÈS[d], Yacouba COULIBALY[c], Bouaké BAKAYOKO[b]

a : Université de Man - BPV20 Man - Côte d'Ivoire.

b : Sama Nickel-CI SARL, 2 plateaux Vallons, 28 BP 1467, Abidjan 28, Côte d'Ivoire.

c : LGSM, UFR STRM, Université Félix HOUPHOUËT-BOIGNY d'Abidjan (Cocody) -22 BP 582 Côte d'Ivoire.

d : Université de Franche-Comté (UMR 6249), 16, route de Gray, 25000 Besançon, France.

*Corresponding author: gouedjiemmanuel@gmail.com ; BPV20 Man - Côte d'Ivoire

Abstract

Mineralogical, geochemical and metamorphic characterization of the Samapleu intrusion shows that it is composed of cumulates of mafic and ultramafic rocks. The ultramafic unit resulted from a single and progressively evolved primitive magma. The mafic unit could have evolved from the same magma or would have formed following a second, more evolved magma injection. The data and signature of major, trace elements and REE of mafic intrusion indicate that it is of basaltic composition with a low Ti and high content of MgO. In addition, it is formed by fractional crystallization under the impingement of a mantle plume at the base of the continental crust inducing textural and mineralogical characteristics of high metamorphic grade with a low level of contamination.

Contact metamorphism is represented by hybrid lithofacies composed of mixtures of mafic igneous and aluminous semipelitic rocks with ultrahigh temperature (T= 850°C ± 100°C and P = 7.5 ± 1 Kbar), which confirm the establishment of this intrusion at the base of the continental crust (ca. 22 km). Therefore, the Paleoproterozoic age (2.09 Ga, age U/Pb on rutile) of the Samapleu intrusion would imply that the intrusion could be coeval of the plume-related ocean flood basalts of the Birimian sequence.

Key-words: Archean-Paleoproterozoic; Yacouba layered complex; Cu-Ni sulfides; Samapleu intrusion; low Ti - high Mg mafic cumulate; ; UHT metamorphism

Introduction

Mining research projects were initiated in 1950 in the Ivory Coast, for the discovery of base metal deposits (Nickel, Copper and Cobalt), platinum group elements (PGE) and chromite. Thus, since 1976, the national company for the mining development (SODEMI) discovered the first Ni-Cu sulfide mineralization associated with the mafic and ultramafic rocks at Samapleu (Western Ivory Coast).

Ouattara (1998) characterized this rock association as a mafic-ultramafic complex, which contains a magmatic deposit rich in sulfides from Ni, Cu and PGE. In this article, this association is considered to be composed of cumulate units of stratified type, which were disrupted by faults in minor deposits. The study subject is the deposit "Samapleu ". Following Ouattara (1998), this igneous body would represent an intraplate body with a tholeiitic signature and would have been set up at paleoproterozoic.

After a long inactivity period in the Samapleu region from 1998 to 2009, mining exploration resumed with the characterization again of Samapleu mafic-ultramafic intrusion. This intrusion is composed of three assemblages: Samapleu Main (SM): Samapleu Extension 1 (E1) and Yorodougou occurrence (Yo) that belong to the Yacouba complex. Indeed, the Samapleu intrusion is a feeder dyke of the Yacouba complex which allowed the establishment of the Ni-Cu and EGP sulfide mineralization of the complex(Gouedji *et al*. 2014).

The Yacouba layered complex forms dismembered and stretched assemblages that extends for more than 25 km long corridor from Yepleu - Bounta to Samapleu -Yorodougou village. It consists of layered assemblages composed of mafic and ultramafic sequences and locally magnetite rich anorthosite units.

This diversity of mafic-ultramafic sites (Samapleu Main, Extension 1, Yorogoudou, Yepleu, etc.) induces the need to characterize the Yacouba complex entirely.

Furthermore, the Samapleu intrusion has petrographic markers of high / ultrahigh-temperature metamorphism and coeval deformation (Gouedji *et al*. 2014, 2018a).

Thus, the geochemical and metamorphic data analysis of the Samapleu intrusion allows a better understanding of the geodynamic context of this intrusion (2.09 Ga), which is mineralized in Ni, Cu and PGE sulfide and emplaced in the archean domain 2.8 Ga.

Finally, this can be a contribution to the understanding of the geology of the Archean domain of Man and source of comparison with other mafic-ultramafic layered intrusive complexes around the world.

This article focuses specifically on the petrological (igneous), geochemical and metamorphic characteristics of the Samapleu intrusion (SM et E1) and its relationship with the granulite gneiss host to understand the P-T conditions of the intrusion and recrystallization of Samapleu complex.

1. Geological setting

The Samapleu intrusion is located in the West African Craton (WAC) which comprises two large shields (the Leo-Man rise in the south and the Reguibat rise in the northwestern Africa), limited by the Neoproterozoic and Mesozoic Taoudeni basin (Fig. 1a, Berger *et al.* 2013). In Ivory Coast, the Man-Leo rise (Fig. 1a) consists of the Kenema-Man Archean domain to the west and the Paleoproterzoic Birimian domain to the east. The Kenema-Man domain was affected by two main events (magmatic and tectono-metamorphic events orogenies); the Leonian (3.3–3.0 Ga) and the Liberian (2.9-2.7 Ga; Camil 1981, 1984; Kouamelan *et al.* 1997) while the Birimian domain took place during the Eburnean (2.2–2.0 Ga; Pitra *et al.* 2010). The Archean sensu stricto (ss), to the north of Danane-Man shear zone (Fig. 1b) is composed of granulitic gneisses (3.05 Ga) and charnockites (2.8 Ga ; Kouamelan *et al.* 1997; Thiéblemont *et al.* 2001; Barth *et al*. 2002; Thiéblemont *et al.* 2004; Peucat *et al.* 2005; Pitra *et al.* 2010; Gouedji *et al.* 2014). In this northern part, Liberian granulitic metamorphism (around 2.8 Ga, T = 750-850°C, P = 5 to 8 Kbar) has been described (Camil 1984; Kouamelan 1996). According to Kouamelan *et al.* (2015), an age of 3207 ± 7 Ma (U–Pb on zircons) obtained from the tonalitic gneiss of Balmer (TGB), in the SASCA area (name from the Sassandra and Cavally Rivers) of south-western Ivory Coast could constitute the protolith of the granulitic gneisses and charnockites of the Man area (Samapleu intrusion host). Subsequently, the Kenema-Man domain was severely reactivated in some places during the Eburnean tectono-metamorphic event, contemporary with the genesis of the Birimian formations (Kouamelan *et al.* 1997; Thiéblemont *et al.* 2004; Gouedji *et al.* 2014; Kouamelan *et al.* 2015; Kouamelan *et al.* 2018).

The Yacouba mafic and ultramafic layered complex intruded within Archean granulitic gneisses, is localised to the north of Danane-Man shear zone, in the Biankouman-Sipilou area (Fig. 1b). This area is generally hilly with a challenging topography with alteration profiles locally exceeding 40 m. The geological map (Fig. 2) summarizes structural and geological information from relatively poor surface exposures and knowledge from geophysical surveys and drill holes. The Archean country rocks in the Samapleu and Santa areas display a NE-SW regional foliation steeply dipping 70° to 90° towards SE or NW; in the Bounta area, the

foliation is sub-horizontal to slightly inclined. The magnetite rich unit which forms a marker horizon, shows thin, folded and dismembered layers whose S0-S1 structures vary from 020° to 080° in the Santa area, 030° to 105° south of Bounta and 040° to 340° NE of Bounta. These data suggest that the Yacouba complex was deformed by a regional dome and basin pattern, as pictured by the distribution of the lithologies (Fig. 2) (Gouedji *et al.* 2014). The complex sequences form dismembered and stretched assemblages along a corridor of more than 25 km from Zeregouine - Yepleu - Bounta in the southwest to Santa and Samapleu to the northeast. It is composed of several ultramafic to mafic rocks including the Samapleu intrusion (Gouedji *et al.* 2014). This layered intrusion comprises peridotite-pyroxenite assemblages (ultramafic) and gabbro-norite - norite assemblages (mafic). These assemblages are typically rich in nickel-copper sulfides along with Platinum Group Minerals (PGM). They locally contain massive chromite layers observed at surface such as the one within the Yepleu intrusion. On the other hand, the mafic assemblages composed of gabbro-norites - gabbros - anorthosites - hypersthene diorites intercalated in pyroxenites - magnetite anorthosite assemblages as observed in the Zeregouine, Yepleu, Bounta and Santa areas (Fig. 2).

The original mafic-ultramafic Samapleu intrusion has been tectonically dismembered and crops out in different places: (i) Samapleu Main area (SM) (Ouattara 1998), (ii) Samapleu 1 extension (E1), 500 m northward of SM (Sama Nickel-CI 2014), and (iii) Yorodougou (Yo), 5 km eastward of SM. These stratabound mafic and ultramafic bodies are generally parallel to the NE regional foliation. The E1 intrusion extends over 2 km in surface and its thickness varies between 50 m and 200 m. Its layering has a NE-SW strike and dips 70°-80° to the SE. The Yorodougou intrusion strikes ENE-WSW, is 1.5 km long in surface and dips 70°-80° to the SE (Fig. 2). Based on the surface geomorphology, the Samapleu section seems to form a fold hinge with a subvertical axis and an axial plane parallel to the regional foliation (Gouedji *et al.* 2014).

2. Sampling and analytical techniques

The mineralogical, geochemical and metamorphic characterization of the Samapleu intrusion was possible by use sampling methods, analytical techniques and software.

More than 35,000 meters of drilling completed by Sama Nickel-CI company have been described macroscopically. More than one hundred rock samples have been taken from the boreholes for the fabrication of polished thin sections of which about seventy are presented in this article to refine the mineralogical and metamorphic characterization of the different formations (Table 1 and 2).

A total of thirty nine (39) whole-rock samples from lherzolite (4) units, olivine websterite (9), websterite (9), plagioclase websterite (4), gabbro-norite (4) and hybrid lithofacies (9), were collected from Samapleu intrusion (SM and E1) boreholes. These rocks were analysed for major and trace elements, using techniques described by Carignan *et al.* (2001) for the geochemical study. Firstly, the rocks were broken and then crushed in a metal jaw crusher (Retsch PM200 type) at the Chrono-Environment Laboratory of the University of Franche-Comté followed by a porphyrisation to obtain a granulometry of less than 80 μm. Then at the Laboratory of the Petrographic and Geochemical Research Center (CRPG) at Vandoeuvre (Nancy - France), the samples were melted with $LiBO_2$ and dissolved in HNO_3 acid. The major elements were analyzed with optical emission spectrometry (ICP-OES Icap 6500 with radial flare) and minor and trace elements by mass spectrometry (ICP-MS X7 from Thermo). The limit of detection is calculated as 6 times the relative standard deviation over 100 measurements of preparation blanks (Table 3 and 4). Measurement uncertainty is calculated for 200 mg of prepared sample. It becomes important (> 25%) over a concentration range between the limit of determination and the lowest concentration for which a percentage of error is indicated.

In addition, these rocks being considered cumulates, their geochemical data were processed according to the methods of calculation and determination of the parent liquids of Chai & Naldrett (1992) and Bédard (1994) whose protocol was described by Gouedji *et al.* (2014).

The metamorphic characterization of the hybrid lithofacies of the Samapleu intrusion through the estimation of the conditions (Pressure - Temperature) was carried out using the perplex software. The use of this software required the acquisition of petrographic, geochemical total rock data as well as data on the mineral chemistry of the hybrid lithofacies rocks. To model of the phase relations, a phase diagram section has been computed in the SiO_2-Al_2O_3-FeO-MgO-CaO-K_2O-Na_2O-TiO_2-H_2O system, using Perple_X_6.6.6 with the updated 2002 version of the internally-consistent thermodynamic database of Holland & Powell (1998). Solid solution models used are presented in table 5.

3. Results

Due to lateritic alteration in Ivory Coast (more than 40 m of laterite thickness) there is not too much outcrops and this makes it necessary to conduct the Samapleu intrusion rocks study from the drilling data. The drilling crosscut the ultramafic unit, the mafic unit and the hybrid unit (remains of the granulite host) (Gouedji *et al.* 2014, 2018a). The results concern

mineralogy, geochemistry and the determination of the P-T-t path of metamorphism through pseudosections of diagnostic assemblages of these units.

3.1 Mineralogy of the Samapleu intrusion rocks

Ultramafic unit of the Samapleu intrusion is composed of peridotite, chromitite, spinel websterite, olivine and plagioclase formations (Table 1).

The peridotite is mainly composed of weakly serpentinized lherzolite (Fig. 3a) whose mineralogical composition varies from harzburgite to dunite. Dunite frequently in contact with the host granulitic gneiss is composed of nearly 90 % olivine and 5 % magnetite, bronzite and diopside are in low proportions. Lherzolite is composed of more than 70 % olivine more or less rounded (mineral cumulus; Fig. 3b) with crystals of straight contours for some and undulous extinctions, deformation kinks for others. Olivine is serpentinized by lizardite. Magnetite (second generation) is associated with lizardite within cracks of olivine. Enstatite, bronzite and diopside with undulous extinctions represent less than 15 % of the rock and interstitial pargasite is 5 to 15 % of the rock. Spinels (less than 5 % of the rock and diameter (Ø) = 0.5 to 2 mm) are interstitial and xenomorphic between silicates or rounded within silicates. Some diopside crystals are encrusted with spinel exsolution. Harzburgite has the same characteristics as lherzolite but with a high proportion of orthopyroxene (bronzite and hypersthene; Table 1).

Macroscopically, **chromitite** forms centimetric to decimetric bands and has sharp contacts with the silicate layers (olivine websterite, peridotite) or disseminated grains between the minerals of these layers (Fig. 3c). The chromitite is magnetic of black color, massive and dense. The interstitial black chromite (70 % of the rock) has a net texture around the silicates (Fig. 3d). Bronzite, diopside and augite (Ø = 0.5 to 3 mm) have undulous extinctions, olivine and chromite spinel are frequently associated and the rounded olivine (less than 5 % of the rock, Ø < 1 mm) is surrounded by chromite (Gouedji *et al.* 2018b). Irvine (1975, 1977) shows that chromite may crystallize with olivine at the beginning of the fractionation of a primitive magma, like at Samapleu. Anorthite, anhedral, medium size, in places with undulous extinction is less frequent, pargasite interstitial and phlogopite rare.

Macroscopically, **spinel websterite** forms centimetric to decimetric bands and presents the same macroscopic aspects like chromitite but with less chromite and more spinels. Spinels (second most abundant mineral, 30 to 40 %) after pyroxenes differ from chromite by their frequent green color. Spinels are associated with magnetite and ilmenite. Gradual contacts with other lithologies are more observed while sharp contacts are less frequent.

In **olivine websterite**, bronzite (40 % of the rock) has in places, straight or sub-rounded contours with undulous extinctions, deformation kinks and surrounded by margins of pargasite.

These grains generally have diameters of 1 to 3 mm but may have a large size (Ø = 2 to 3 cm) encrusted with olivine or diopside. Olivine (10 to 20 % of the rock, Ø = 0.5 to 2 mm) is subhedral and acicular, weakly serpentinized associated with magnetite. Bronzite, diopside are intercumulus and spinels are interstitial or included in pyroxenes; the pargasite is anhedral, around olivine and pyroxenes reaching up to 10 to 15 % in this rock and phlogopite is less present.

The **websterite** is macroscopic massive and dark green (Fig. 3e). It consists mainly of bronzite (70 % of the rock) and diopside (less than 20 % of the rock), euhedral to subhedral with subarround contours, sizes (generally Ø = 0.5 to 2 mm and locally Ø = 0.5 to 2cm). In places, bronzite and diopside form polygonal crystals, undulous extinction, deformation kinks and triple points of about 120° and attest a granoblastic texture of metamorphic origin. In places, rare small polygonal crystals (Ø = 0.5 to 1mm) are juxtaposed to some of average size (Ø = 2 to 5 mm) just like polygonal which could be due to recrystallization at high temperature. Anhedral spinels are interstitial, rounded, in inclusion or in exsolutions in pyroxenes (Fig. 3f). Olivine, scarce, with fine and rounded crystals, is poecilitic in inclusion in pyroxenes and pargasite reach up about 15 % of the rock in places.

In websterite, plagioclase (anorthite - Ø = 0.5 to 2 mm) anhedral to subhedral is interstitial to diopside and bronzite. It represents 10 to 15 % of the rock, resulting in the **plagioclase websterite**. Also, pargasite is abundant in this lithology as phlogopite is increasingly present.

The **mafic unit** consists of gabbro-norite, norite and anorthosite formations (Table 1). The **gabbro-norite** is macroscopically massive of green-white color (Fig. 3g). It consists of essentially bronzite, diopside, bytownite and pargasite (Fig. 3h). Sub-rounded bronzite (5 to 40 % of the rock) with a diameter of 3 mm to 2 cm, presents in places, undulous extinctions, folding bands and is surrounded by margins of amphibole. Diopside (less than 15 % of the rock) is scarce in places, resulting in the norite. In **norite**, bytownite and pyroxenes are associated. Subhedral bytownite and interstitial provides 30 to 40 % of the rock and several crystals have undulous extinctions. The proportion of plagioclase varies and reaches 80 to 90 % of the rock and forms the **anorthosite**. Plagioclase and pyroxenes show in anorthosite like gabbro-norite**,** a phlogopite reaction ring and, in places, euhedral to subhedral phlogopite.

The anhedral and interstitial pargasite between pyroxene and plagioclase can reach 5 to 10 % in the rock.

Massive macroscopically, **the hybrid lithofacies** is gray in color (Fig. 4a). Mineralogical composition varies from the noritic to the anorthositic pole (Table 2). Plagioclase (labrador 30 to 50 % of the rock) has crystals of variable size (Ø = 0.5 to 5mm), euhedral to subhedral, rounded contour, with undulous extinction, associated with orthopyroxene (Opx) and sapphirine (Fig. 4b). Moreover, other small and polygonal crystals (Ø = 0.5 to 1mm) are juxtaposed to some of average size (Ø = 2 to 5 mm) just like polygonal involving a recrystallization at high temperature. Bronzite (10 to 30 % of the rock) and sapphirine (10 to 20 % of the rock) are anhedral to subhedral, in places are associated with garnet, biotite, sillimanite, amphibole and cordierite. Green spinel consisting of hercynite (very variable proportion; less than 10 %) is frequently associated with sapphirine. Ilmenite, rutile and biotite (less than 5 % of the rock) are euhedral. Some fine crystals of quartz, zircon and corundum have been observed. The garnet (Ø = 1 to 7 mm) euhedral to subhedral, is also present in places.

3.2 Geochemistry of the Samapleu intrusion rocks

Results of major, trace elements and REE analyses of mafic, ultramafic, and hybrid lithofacies are presented in table 6 and 7. The mafic-ultramafic and hybrid lithofacies data are analyzed separately and several geochemical signatures are observed (Figure 5 to 9).

Major oxide geochemistry

The mafic-ultramafic rocks

The MgO contents range from 10 wt.% to 32 wt.% in the mafic-ultramafic rocks.

Ultramafic rocks (lherzolite, olivine websterite, websterite and plagioclase websterite) contain high contents of MgO and Fe_2O_3 and SiO_2 contents are relatively low. Al_2O_3 and CaO contents are low in lherzolite however, in olivine websterite, websterite and plagioclase websterite CaO and Al_2O_3 contents are relatively high. In gabbronorite (mafic rock), the SiO_2 contents vary slightly with low contents of MgO and Fe_2O_3. The contents of Al_2O_3 and CaO are very high.

All mafic-ultramafic rocks of the Samapleu intrusion are very low in TiO_2, Na_2O, MnO and K_2O (Table 6).

Values of some minor elements such as Ni, Cr are abundant in places and Co is moderately high (Table 6).

In the diagram of major elements versus MgO (Fig. 5), showing the effects of fractionation during magma evolution, MgO decrease in crystals formed during fractionation in cumulates. Figure 5 reveals two different trends observed from lherzolite to plagioclase websterite and then to gabbro-norite.

The first, from lherzolite to plagioclase websterite, is characterized by increase of SiO_2 (38.16 - 50.91 wt.%), Al_2O_3 (2.2 - 11.37 wt.%), CaO (0.75 - 7.7 wt.%) and a decrease in Fe_2O_3 (21.9 - 12.35 wt%). TiO_2 and Na_2O also increase, but their values vary considerably within the same lithology and remain very low (Contents of TiO_2 and Na_2O range respectively from 0.05 wt.% to 0.32 wt.% and from 0.1 wt.% to 1.07 wt.%). This is probably due to the accumulation of olivine, pyroxene and plagioclase which crystallized from primitive liquids which subsequently evolved (Gouedji *et al.* 2014).

The second trend of plagioclase cumulates of gabbro-norite shows slight decrease in the contents of MgO (12.91 to 10.59 wt.%) and Fe_2O_3 (8.31 to 6.64 wt.%). This trend is accompanied by a slight increase in SiO_2 (46.67 to 47.77 wt.%), CaO (9.87 to 14.15 wt.%), TiO_2 (0.19 to 0.22 wt.%), Na_2O (0.84 to 1.58 wt.%) and especially Al_2O_3 (15.72 to 19.66 wt.%) which increases more significantly. In addition such variations reflect the evolution of the composition of crystals that precipitate (pyroxene and plagioclase). also, the Al_2O_3 contents become abnormally high, reflecting the possible contamination by the country rocks.

The hybrid lithofacies

The hybrid lithofacies shows a great variability of the chemical compositions that could represent different degrees of metasomatism of the host rocks. Thus SiO_2 contents vary slightly; the MgO and Fe_2O_3 contents show wide variation as well as the Al_2O_3 and CaO contents. The hybrid lithofacies is very low in TiO_2, Na_2O, MnO and K_2O contents (Table 7). Also, this wide variability in the geochemistry of the major oxides of the hybrid lithofacies would reflect the possible mixing of the mafic-ultramafic intrusion and the country rocks.

Trace element Geochemistry

The mafic-ultramafic rocks

The values for Nb, Ta and Zr contents are very low, close to their detection limit, this most likely results from cumulative effects in the formation of the different rocks of the Samapleu intrusion. The anomalously high values for Ni (592 - 3020 ppm) and Cu (76 - 2355 ppm) in

the lithologies (websterite, plagioclase websterite, olivine websterite) reflect the presence of sulfides (Table 6).

MORB-normalized Multi-element patterns show an overall enrichment in lithophilic elements (LILE, Ba, Rb, Th), a general negative Nb and Ta anomaly highlighting a weak positive anomaly in La and Ce. Also, we note an overall slight depletion of MREE (Sm, Tb), HREE (Dy, Yb) and a depression of HFSE (Hf, Zr) depending on the samples. Depending on the samples, Ti and Eu may have a positive or negative anomaly (Fig. 6).

The hybrid lithofacies

MORB-normalized Multi-element patterns generally indicate a high enrichment in LILE and Th, which could indicate probable injection of the continental crust by contamination. A general depression in Nb, Ta and a general negative anomaly in Sm, flat spectra of HREE (Dy, Yb), moderate enrichment of HFSE (Hf, Zr) are observed (Fig. 7).

REE geochemistry

The mafic-ultramafic rocks

Chondrite-normalized REE patterns of the Samapleu rocks are generally flat (REE concentrations between one to a ten times chondrite values with (La/Yb)n which varies between 0.17 and 3.67. The rocks are slightly enriched in LREE ((La/Sm)n = 0.16 - 3.80) and relatively constant in HREE ((Dy/Yb)n = 0.50 – 1.16). Plagioclase rocks indicate a positive Eu anomaly (Fig. 8 ; Table 6).

The hybrid lithofacies

Chondrite-normalized REE patterns are shown a strong enrichment in LREE, (LREE – 100 time chondrite values with (La/Sm)n = 6.20 - 15.85) and (La/Yb)n = 3.26 - 108.37 but display a fairly flat spectrum for HREE (Dy/Yb)n = 0.42 - 1.43; Fig. 9 ; Table 7).

3.3 Metamorphism

The hybrid lithofacies sample (SM24 (4) 33) was used to quantify the pressure and temperature conditions of emplacement of the Samapleu intrusion. This sample consists of about 10 to 15 % of garnet, 20 to 30 % of plagioclase (Labrador), 30 to 40 % of orthopyroxene, 5 to 10 % of sapphirine, 2 to 5 % of biotite, 10 to 15 % of spinel (Fig. 10a). In places, it contains 1 to 3 % of opaque minerals (rutile, ilmenite) and traces of sillimanite and cordierite. Rutile is generally in inclusions within plagioclase. Microscopic observation

shows symplectite texture with spinel-sapphirine association and spinel in the center which is surrounded by garnet, plagioclase or cordierite (Fig. 10a).

Orthopyroxene occurs in the matrix as large euhedral crystals with abundant plagioclase and euhedral biotite crystals (Fig. 10b). In contrast, garnet forms irregular porphyroblasts that contain in their core large and partially resorbed spinel inclusions suggesting that they were developed at the expense of spinel. Garnet also contains orthopyroxene and plagioclase inclusions. We therefore suggest that the primary metamorphic assemblage consists of orthopyroxene, plagioclase and spinel (Fig. 10b) and that garnet post-date this assemblage. Sapphirine is observed as a thin moat surrounding spinel (Fig. 10a and c) and also generally forms at the expenses of OPX (Fig. 4b). Sapphirine is best developed when spinel is in contact with matrix plagioclase but it also occurs, in significantly less amount, when spinel is included in garnet. These coronitic texture suggests that sapphirine post-date the peak metamorphic assemblage. To model these phase relations, a phase diagram section has been computed in the SiO_2-Al_2O_3-FeO-MgO-CaO-K_2O-Na_2O-TiO_2-H_2O system. The bulk composition used in the phase diagram is presented in mol% in figure 11.

The phase diagram in Figure 11a, shows that peak temperature assemblage (Opx, Pl, Bio, Sp, Ilm) is restricted to ultra-high temperature conditions above 980 °C for a large range in pressure (from 3 to 10 kbar). Development of garnet and sapphirine at the expense of spinel requires cooling down to temperature of 800 °C at pressure higher than ~ 7 kbar in order to stabilize garnet. In order to better constrain the P-T conditions, the phase diagram section has been contoured for molar Ti content and XMg of biotite, pyrope and almandine content of garnet, molar Al_2O_3 content and XMg of Orthopyroxene (figure 11b,c,d). Al_2O_3 content of orthopyroxene above 0.17 mol per formula unit is consistent with peak temperature above 1000°C while XMg of 0.72 - 0.73 indicates a pressure greater than ~ 9 kbar. Garnet composition (X_{Alm} = 46 to 47 % and X_{prp} = 46 and 48 %; Table 8) is consistent with cooling at pressure ranging from 6.6 to 8.4. Although biotite belongs to peak metamorphic conditions XMg (0.75 - 0.78) and TiO_2 content (0.18 - 0.21) suggest that they were reequilibrated during cooling from 1020 to 780 °C.

To conclude, phase relation modeling suggests that the hybrid lithofacies located at the contact of the Samapleu intrusions, preserves evidences of ultra-high temperature conditions of at least 1000 °C and pressure of ~ 9 kbar, followed by near isobaric cooling down to 750 – 800 °C at 7 - 8 kbar. We suggest that these metamorphic condition and the development of the hydrid lithofacies are coeval with emplacement of the Samapleu intrusion.

4. Discussion

Cumulate of a Basaltic Magma

The Samapleu intrusion, part of the Yacouba layered complex, comprises ultramafic units (peridotite, pyroxenite and chromitite) and mafic units (gabbronorite, norite, anorthosite) and are composed of cumulate rocks. Although these rocks inherited adcumulate, mesocumulate or orthocumulate textures (Ouattara 2018; Gouedji *et al.* 2014), in some places, the pyroxenes and plagioclases show undulous extinction and deformation kinks (markers of solid-state plastic deformation), and triple points of about 120° (markers of recrystallisation by static annealing) (Ferreira *et al.*1998; Pronost 2005). According to the petrography and mineralogy, the evolution of these cumulative sequences indicates the following order of emplacement: (i) peridotite and chromitite; (ii) pyroxenitic set, finally (iii) mafic sequences (Gouedji *et al.* 2018a). This observations would imply a fractional crystallization of these formations.

Furthermore, minerals such as olivine, Opx, Cpx and amphibole present in these lithologies have relatively low values of Cr_2O_3, Na_2O and TiO_2, moderate iron enrichment in Cpx and high values in MgO of the minerals. According to Gouedji *et al.* (2018), the crystallo-chemistry of minerals indicate that this intrusion would be formed from a mantle magma of basaltic composition by fractional crystallization. In addition, the presence of olivine, Opx (enstatite and bronzite), Cpx (diopside) and the regular presence of spinel in the peridotites would imply that these ultramafics would be formed at UHT and MP or would have been affected by a metamorphism with the same characteristics (Bucher & Grapes 2011). Similarly, the assemblage (plagioclase, Opx, Cpx and amphibole) observed in mafic rocks, indicates that (re) - crystallization occurred under conditions of high temperature (equivalent to the granulite facies) (Della *et al.* 2011; Bucher & Grapes 2011).

Nature of the primary magma

The correlation of MgO content with SiO_2, Fe_2O_3, Al_2O_3, CaO, TiO_2 and Na_2O for layered rocks of the Samapleu (Fig. 5) confirms to the sequence of crystallization of cumulus minerals. Relatively low CaO and TiO_2 contents in ultramafic rocks are consistent with the predominance of orthopyroxene over clinopyroxene in the layered rocks (Della *et al.* 2011). This major-element distribution in ultramafic to mafic rocks of Samapleu suggest that lherzolite, olivine websterite, websterite and plagioclase websterite have most likely resulted from a single and progressively evolved primitive magma. The gabbro-norite sequence could

have evolved from the same magma but it is also possible that it was formed following a second, more evolved magma injection (Gouedji *et al.* 2014).

The estimation of the parent magma composition from the major elements was done according to the approach proposed by Chai & Naldrett (1992) used by Gouedji *et al.* (2014). As the Samapleu main area (SM) has limited available analytical data, this method was applied only to the data from Extension 1 area (E1). Using that approach, the results presented by Gouedji *et al.* (2014) indicate a parent magma composition of 10 % MgO, 11 % FeO, 53 % SiO_2 and 0.65 % TiO_2 obtained. Also, the minor, trace elements and REE contents have been recalculated for the Samapleu (SM and E1) rocks according to the method of Bédard (1994) used by Gouedji *et al.* (2014). According to this method, a fraction of trapped liquid (TM) was considered at 5% because the microscopic observations of the Samapleu rocks (crystals euhedral to subautomorphous, well crystallized even the interstitial crystals) shown that liquid phase is almost not observable. It is shown (TM < 5 %) significantly influences the composition of the calculated liquid (Charlier *et al.* 2005) and TM of the order of 20 % would imply an abundant presence of liquid in the cumulates.

Thus, the parent liquid has a ratio of Nb/Ta varying from 2.75 to 29.24 (with a mean around 11) and a ratio of Zr/Hf comprised between 19.00 and 59.14 (average around 39; Table 9). These ratios are different from those of primitive mantle magmatic liquids whose Nb/Ta ratio is around 17.4 ± 0.5, (Jochum *et al.* 1997; Barth *et al.* 2000) and Zr/Hf ratio around 36.30 (Hui *et al.* 2011). These variations could be related to fractional crystallization during the establishment of magma (Hui *et al.* 2011) and also to cumulative effects.

The Ni (148-417 ppm) and Cr (174-837 ppm) contents obtained from lherzolite and olivine websterite in equilibrium with the primary magma, using Bédard method (1994), are compatible with the magmatic liquid. MgO content, determined by the method of Chai & Naldrett (1992) is high. In fact, major and minor element compositions in addition to trace elements and REE are typical of high MgO and low Ti basalts. These values are similar to those characterized in the Ni-Cu, EGP intrusions of Jinchuan (China, Chai & Naldrett 1992) and Nebo-Babel (Australia, Godel *et al.* 2011).

Features of the primary magma and assimilation of country rocks (granulite facies)

Chondrite-normalized equilibrium liquid REE patterns (TM = 5 %) shown spectra parallel to each other that might indicate a common source with a strong enrichment in LREE (LREE = 10 to 100 time chondrite values with (La/Sm)n = 0.59 - 13.51) and in (La/Yb)n = 0.62 - 20.06 but display a fairly flat spectrum for HREE (Dy/Yb)n = 0.84 - 1.97) (Fig. 12).

MORB-normalized Multi-element patterns indicate spectra almost parallel to each other with strong enrichments in LILE (Ba, Rb and Th). It shows a negative anomaly in Nb and Ta as well as flat spectra of MREE (Sm, Tb), of HREE (Dy, Yb) and a HFSE depression (Hf, Zr) (Fig. 13).

Negative (Ta and Nb) and positive LILE anomalies are the main features of low Ti basalt in continental shelf basalt provinces (Arndt *et al.* 1993; Lassiter & DePaolo 1997; Arndt *et al.* 1998; Baker *et al.* 2000; Puffer 2001; Ewart *et al.* 2004a, b), they reflect the contamination of a mantle magma by crust during its ascent to the surface (Arndt *et al.* 1993, 1998 ; Zhou *et al.* 2008). Also, they could evidence a magma resulting from a subcontinental lithospheric mantle metasomatised by silicates in processes of melted old subductions (Zhao & McCulloch 1993 ; Lassiter & DePaolo 1997). Indeed, Gouedji *et al.* (2014) indicate an enrichment in Th, Ba, Rb with a depression in Nb, Ta, Ti of the granulite country rocks (Samapleu intrusion host) showing their belonging in the continental crust.

Wooden *et al.* (1993), Arndt *et al.* (1998), Baker *et al.* (2000), Zhou *et al*. (2008) have shown that low Ti basalts observed in continental shelf basalt provinces have been particularly affected by crustal contamination and that their chemical compositions reflect the assimilation of crustal rocks by primary mantle (picritic) melted. As well, in the Nebo-Babel zone (Australia), modeling on low Ti basalts (Boudreau 1999) with the hypothesis of a picritic magma assimilated from 0 to 30 % of the lower crust (P = 6 Kbar, fO_2) resulted in a composition of SiO_2 < 48, MgO = 10-13 %, TiO_2 = 0.70-1.1 % and FeO = 11.9-12.5 %, (Godel *et al.* 2011). The ratios of Th/Yb (0.8 - 5), Nb/Th (0.4 - 2.1) and Zr = 40 - 50 ppm (average 142 ppm Zr in continental crust; Rudnick & Gao 2004) obtained are indicators of low levels of crustal contamination.

Comparing the values of the Nebo-Babel intrusion with those of Samapleu ((SiO_2 = 53 %, MgO = 10 %, TiO_2 = 0.65 %, FeO = 11 %, Th/Yb = 0.36 - 7.02, Nb/Th = 0.59 - 13.51) and Zr = 11.05 – 90.55 ppm (mean around 40 ppm, Table 9)); these values are almost similar and indicate that the Samapleu intrusion appears to have undergone a low level of contamination.

The low Nb contents, although characteristic of a subduction context, are, with the Ta depletion and Ba enrichment, Rb, Th in the case of Samapleu are characteristic of a mantle plume with assimilation by the surrounding rocks granulite. Also, Ba enrichment was thought to be derived from the charnockite contamination of the mafic complex of Ivrea Verbano in Italy (Sinigoi *et al.* 1994). In the mantle plume activity, at the base of the upper mantle, the impact of a plume causes the melting of the shallow envelope and leads to the formation of basaltic to picritic magmas with high MgO and low Ti contents. These magmas

will assimilate a small proportion of the lower granulitic continental crust during their emplacement and rise to the surface (Fig. 14), as observed at Samapleu with the assimilation of granulite causing the formation of hybrid lithofacies (Anhaeusser 2015). Indeed, this wide variability in the geochemistry of the major oxides and negative anomalies (Ta and Nb), high enrichment in LILE and Th observed within hybrid lithofacies, confirm that this formation is the consequence of the contamination of the Samapleu intrusion by the surrounding granulites during its ascent to the surface (Arndt *et al.* 1998 ; Zhou *et al.* 2008). As well, the omnipresence of the amphiboles (tschermackite, pargasite, hornblende) in the Samapleu intrusion rocks (Gouedji *et al.* 2018a) could be explained by the contribution of the fluids by the host rocks during the formation and the rise of the magmas (Zhao & Zhou 2006 ; Sanghoon *et al.* 2012). Moreover, lizardite (serpentine formed at temperatures below 300 °C, Schwartz *et al.* 2012), which is ubiquitous in peridotites, appears to have been formed either by weathering alteration of olivine or by metamorphic retrogression or metasomatism during the injection of late fluids.

Emplacement and metamorphism

High MgO levels indicate that Samapleu magmas were relatively hot (Precambrian thermal gradient = 50 °C/Km; Chardon 1997). This implies emplacement of the intrusion in the lower crust at a depth of about 22 km with a crystallization temperature of Samapleu magmas around 1100 to 1200 °C.

Indeed, deformation kinks, undulous extinctions, recrystallization textures and spinel exsolutions in pyroxenes of the intrusion evidence that the intrusion has formed and set up at ultra-high temperature under lithospheric mantle and in the base of the continental crust (Frets *et al*. 2012; Della *et al.* 2011; Cabanes & Mercier 1988; Desnoyers 1975); as well as the presence of hercynite and chromite magnetite (minerals of high grade metamorphism; Barnes & Roeder 2001).

The metamorphic study indicates that the hybrid lithofacies (observed in contact with the intrusion and its granulite host) preserves evidences of ultra-high temperature conditions of at least 1000 °C and pressure of ~ 9 kbar, followed by near isobaric cooling down to 750 – 800 °C at 7 - 8 kbar. This is indicative of a metamorphic recrystallization of granulite host under utra-high temperature and medium pressure (T = 850 °C ± 100 °C and P = 7.5 ± 1 Kbar) (Gouedji 2014). This recrystallization is certainly related to the remobilization (assimilation) of this granulite during the ascent of the mafic-ultramafic mantle material with a high MgO content. The aluminous and magnesian materials, which could result from a mixing between

the parent magma and its host, would have formed paragenesis with sapphirine, garnet and spinel ± sillimanite ± cordierite. This aluminous mineral assemblage is common in the high-grade pelitic sequence (Bucher & Grapes 2011).

Thereby, mafic-ultramafic Samapleu body is injected at a temperature of (1200º to 1100° C), producing a high-grade contact metamorphism in the host rocks (thermal peak between 1000 and 800º C). Its protracted crustal residence stabilizes its mineral associations to the same metamorphic conditions. The cooling is fast between 1100 and 1000 but slows down when it balances its temperature with that of the host rocks.

An Eburnean age (2.09 Ga, age U / Pb obtained on rutile) was obtained on hybrid lithofacies and which would be the age of metamorphism having produced these formations (Gouedji *et al.* 2014).

Indeed, the closing temperature of rutile in granulite-facies rocks is high (higher than 600 °C which can reach 750 °C) and rutile dating would give information about the time of the last metamorphic episode (Zack *et al.* 2011; Bruguier 2009; Vry & Baker 2006; Schärer & Labrousse 2003).

However, Pitra *et al.* (2010) indicate that during the Palaeoproterozoic Eburnean event (2.03 Ga ; age obtained on Sm–Nd garnet – whole-rock), Archean formations to the south of the Man-Danane Fault underwent strong reworking under high-pressure granulite facies conditions. This episode overprints the low to medium pressure Liberian (c. 2.8 Ga) granulite facies metamorphism. These metamorphic (M2) conditions have not been described on Archean formations to the north of the Man-Danane fault where the Samapleu intrusion is located.

In addition, it emerges from the metamorphic study of the country rocks (dated of 2.8 Ga; age U / Pb obtained on zircon; the Samapleu intrusion host) of the Sipilou-Biankouma region that the conditions having affected these rocks would be around (P = 6 Kbar and T = 800 °C; amphibolitic to granulitic metamorphism (M1) at MP and HT) (Baptiste 2013; Gouedji 2014). Such conditions have already been described in the region by other authors (Camil 1984; Caby *et al.* 2000; Berger *et al.* 2013) as being those of granulitic metamorphism linked to the Liberian cycle.

From all of the above, we suggest that the metamorphic conditions (UHT and MP) obtained on hybrid lithofacies and the development of hybrid lithofacies are coeval with the emplacement of the Samapleu intrusion.

Thus, the development of hybrid lithofacies would be linked to a thermal contact metamorphism (M3) caused by the establishment of the Samapleu intrusion within the

granulite host in a lower continental crust at a depth of about 22 km under typical P-T conditions of granulite metamorphism.

The high temperature of the magmas facilitates the assimilation of the country rocks causing the contamination of the magmas. It can also cause contact metamorphism whose effects would be attenuated by regional granulite metamorphism (Sappin *et al.* 2006). This explains the low contamination rate that has affected the Samapleu intrusion linked to an emplacement in the lower crust in a granulite host, affected by regional granulitic metamorphism (Gouedji *et al.* 2014). A crystallization temperature of 1100 to 1200 °C of the Samapleu intrusion can be considered as a signature related to the mantle plume type (Luo *et al.* 2014).

Geodynamic context

The parental melt composition has a basalt rich MgO and low Ti and suggest Samapleu intrusion was formed by melting of the upper mantle under the influence of a mantle plume. Thus, during its ascent, magma has assimilated the granulites country rocks (Fig. 14).

This geodynamic model shows identical features to those of Jinchuan intrusions (China), Ivrea Verbano (Italy) and Nebo-Babel (Australia) observed in continental shelf basalt provinces affected by crustal contamination. At the sub-regional level, it can be related to the emplacement of the plume-type basalts of Birimian sequences (Abouchami *et al.* 1990) described in the Eburnean domain. As well, it could be related to the immense quantities of mafic magmas produced at Birimian in West Africa (Thiéblemont *et al.* 2004; Lompo 2009, 2010; Pitra *et al.* 2010), when 2.09 Ga considered as the age of emplacement of Samapleu intrusions. Gouedji *et al.* (2014) obtained an age of 2.09 Ga (Age U/Pb on Rutile) from the hybrid lithofacies considered as the contact granulite metamorphism (M3) age. Also, the regional granulitic metamorphism (M1) of the host rock of the Samapleu intrusion, has been dated 2.8 Ga (Camil 1984; Kouamelan 1996; Gouedji *et al.* 2014).

Thus, the history of magmatic and metamorphic evolution in the Sipilou-Biankouma region can be summarized as follows; a continental accretion (formation period and stabilization of the continental crust with tonalite-trondhjemite-granodiorite formation (TTG) would have been formed between 3.61 Ga and 3.3 Ga (inherited age, Gouedji 2014). It was followed by a Leonean orogeny of 3.22 to 2.92 Ga (inherited age) characterized by the presence of gray gneiss (Camil 1984). Then, magmatic and / or metamorphic Liberian events (2.78 Ga, metamorphic age) occurred with the formation of granulite felses (Gouedji *et al.* 2014). Finally the establishment of a series of mafic-ultramafic intrusion of the Yacouba complex,

including that of Samapleu (2.09 Ga) within the gneissic granulite rocks and containing Ni-Cu and EGP mineralization.

Conclusion

The Samapleu intrusion is in Archean granulitic gneisses (3.6 - 2.78 Ga). This is a cumulate rocks association composed of ultramafic sequences (peridotite, pyroxenite and chromitite) and mafic sequences (norite, gabbro-norite and anorthosite). The ultramafic unit has most likely resulted from a single and progressively evolved primitive magma and underwent fractional crystallization. The mafic unit could have evolved from the same magma but it is also possible that it formed following a second, more evolved magma injection.

Major element compositions of the recalculated liquid (10 % MgO, 11 % FeO, 53 % SiO_2 and 0.65 % TiO_2) of the Samapleu intrusion indicate it is formed from a mantle-derived magma of low-Ti high-Mg basaltic composition. The signatures of the trace elements and REE shown that it is affected by crustal contamination with a small assimilation proportion of the granulitic continental crust during its emplacement.

The magma could be placed by underplating and feeding from a mantle plume at the base of the continental crust (ca. 22 km depth; ca. 1100 - 1200 °C temperature).

Contact metamorphism is of ultrahigh temperature and medium pressure conditions. This is confirmed by the hybrid lithofacies mineral assemblages, which indicate a metamorphic recrystallization of ultrahigh temperature and medium pressure in the granulite host (T = 850 °C ± 100 °C and P = 7.5 ± 1 Kbar).

Samapleu intrusion cooled since 2.09 Ga (U-Pb age on rutile), during Birimian time and could be coeval to emplacement of the plume-related ocean flood basalts of the birimian sequence as well as other voluminous mafic magmas contained in the Birimian successions of West Africa.

Acknowledgments

The authors are very grateful to Sama Nickel-CI for funding this work. We are also grateful to SODEMI and the Chrono-Environment laboratory of the University of Franche-Comté (France) who contributed to the realization of this article. We acknowledge that N'Cho Odon Clement (University of Man) helped to improve the language content.

References

Abouchami, W., Boher, M., Michard, A. & Albarede, F. 1990. A major 2.1 Ga old event of mafic magmatism in West Africa: an early stage of crustal accretion. *Journal of Geophysical Research*, **95** 17605-17629.

Anhaeusser, C. R. 2015. Metasomatized and hybrid rocks associated with a Palaeoarchaean layered ultramafic intrusion on the Johannesburg Dome, South Africa. *Journal of African Earth Sciences*, **102,** 203-217.

Arndt, N. T., Czamanske, G. K., Wooden, J. L. & Fedorenkof, V. A. 1993. Mantle and crustal contributions to continental flood volcanism. *Tectonophysics*, **223**, 39-52.

Arndt, N. T., Chauvel, C., Czamanske, G. K. & Fedorenkof, V. A. 1998. Two mantle sources, two plumbing systems: Tholeitic and alkaline magmatism of the Maymecha River basin, Siberian flood volcanic province. *Contributions to Mineralogy and Petrology*, **133**, 297-313.

Baker, J. A., Macpherson, C. G., Menzies, M. A., Thirlwall, M. F., Al-Kadasi, M. & Mattey, D. P. 2000. Resolving crustal and mantle contributions to continental flood volcanism, Yemen: Constraints from mineral oxygen isotope data. *Journal of Petrology*, **41**, 1805-1820.

Baptiste, J. 2013. *Caractérisation structurale et évolution pression-température des assemblages archéens-paléoprotérozoïque du craton de Man région de Biankouma (Ouest de la Côte d'Ivoire).* Master d'écologie appliquée, Université de Franche-Comté.

Barnes, S.-J. & Roeder, L. P. 2001. The range of spinel compositions in terrestrial mafic and ultramafic rocks. *Journal of petrology*, **42**, 2279-2302.

Barth, M. G., McDonough, W. F. & Runick, R. L. 2000. Tracking the budget of Nb and Ta in the continental crust. *Chemical Geology*, **165**, 197-213.

Barth, M. G., Rudnick, R. L., Horn, I., McDonough, W. F., Spicuzza, M. J., Valley, J. W. & Haggerty, S. E. 2002. Geochemistry of xenolithic eclogites from West Africa. Part II: origins of the high MgO eclogites. *Geochimica et Cosmochimica Acta*, **66**, 4325-4345.

Bédard, J. H. 1994. A procedure for calculating the equilibrium distribution of trace elements among the minerals of cumulate rocks and the concentration of trace elements in the coexisting liquids. *Chemical Geology*, **118**, 143-152.

Berger, J., Diot, H., Khalidou, L., Ohnenstetter, D., Féménias, O., Pivin, M., Demaiffe, D., Bernard, A. & Charlier, B. 2013. Petrogenesis of Archean PGM-bearing chromitites and associated ultramafic–mafic–anorthositic rocks from the Guelb el Azib layered complex (West African craton, Mauritania). *Precambrian Research*, **224,** 612-628.

Boudreau, A. E. 1999. PELE - a version of the MELTS software program for the PC platform. *Computers & Geosciences*, **25**, 201-203.

Bruguier, O. 2009. *Géochronologie U-Pb par ablation laser et ICP-MS (LA-ICP-MS): Principes, Complexités et Perspectives*. Ingénieurie de Recherche au CNRS. Géosciences Montpellier, Laboratoire ICP-MS / Université Montpellier II.

Bucher, K. & Grapes, R. 2011. *Petrogenesis of metamorphic rocks*. Springer Science & Business Media.

Camil, J. 1981. Un exemple de metamorphisme prograde de la base du faciès des amphibolites au faciès des granulites dans la région de Man (Ouest de la Côte d'Ivoire). *Compte Rendu de l'Academie des Sciences, Paris*, **93**, 513-518.

Camil, J. 1984. *Pétrographie, chronologie des ensembles granulitiques archéens et formations associées de la région de Man (Côte d'Ivoire). Implication pour l'histoire géologique du Craton Ouest-Africain.* PhD thesis. Université, Abidjan.

Cabanes, N. & Mercier, J.-C. 1988. Chimie des phases minérales et conditions d'équilibre des enclaves de lherzolite à spinelle de Montferrier (Hérault, France). *Bulletin de Minéralogie,* **111, 1,** 65-77.

Caby, R., Delor, C. & Agoh, O. 2000. Lithologie et métamorphisme des formations birimiennes dans la région d'Odienné (Côte d'Ivoire) : rôle majeur du diapirisme des plutons et des décrochements en bordure du Craton de Man. *Journal of African earth,* **3, 2,** 351-374.

Carignan, J., Hild, P., Mevelle, G., Morel, J. & Yeghicheyan, D. 2001. Routine analyses of trace elements in geological samples using flow injection and low pressure on-line liquid chromatography coupled to ICP-MS: a study of geochemical reference materials BR, DR-N, UB-N, AN-G and GH. *Geostandard Newsletter*, **25, 2-3,** 187-198.

Chai, G. & Naldrett, A. J. 1992. The Jinchuan ultramafic intrusion: Cumulate of a high-Mg basaltic magma. *Journal of Petrology,* **33**, 277-303.

Chardon, D. 1997. *Les déformations continentales archéennes : Exemple naturel et modélisation thermomécanique.* Thèse de doctorat de l'Université de Rennes I. Mémoire de Géosciences-Rennes.

Charlier, B. T., Auwera, V. J. & Duchesne, J. C. 2005. Geochemistry of cumulates from the Bjerkreim–Sokndal layered intrusion (S. Norway) Part II. REE and the trapped liquid fraction. *Lithos,* **83**, 255-276.

Della, G. M. E. S., Pimentel, M. M., Ferreira, F. C. F. & De Hollanda, M. H. B. M. 2011. Dating coeval mafic magmatism and ultrahigh temperature metamorphism in the Anápolis–Itauçu Complex, Central Brazil. *Lithos,* **124, 1-2,** 82-102.

Desnoyers, C. 1975. Exsolutions d'amphibole, de grenat et de spinelle dans les pyroxènes de roches ultrabasiques : péridotite et pyroxénolites. *Bulletin de la Société française de Minéralogie et de Cristallographie*, **98, 1**, 65-77.

Ewart, A., Marsh, J. S., Milner, S. C., Duncan, A. R., Kamber, B. S. & Armstrong, R. A. 2004a. Petrology and geochemistry of Early Cretaceous bimodal continental flood volcanism of the NW Etendeka, Namibia. Pt. 1: Introduction, mafic lavas and re-evaluation of mantle source components. *Journal of Petrology*, **45,** 59-105.

Ewart, A., Marsh, J. S., Milner, S. C., Duncan, A. R., Kamber, B. S. & Armstrong, R. A. 2004b. Petrology and geochemistry of Early Cretaceous bimodal continental flood volcanism of the NW Etendeka, Namibia. Pt. 2: Characteristics and petrogenesis of the high-Ti latite and high-Ti and low-Ti voluminous quartz latite eruptives. *Journal of Petrology*, **45,** 107-138.

Ferreira, F. C. F., De Moraes, R., Fawcett, J. J. & Naldrett, A. J. 1998. Amphibolite to granulite progressive metamorphism in the Niquelândia Complex, central Brazil: regional tectonic implications. *Journal of South American Earth Sciences*, **11, 1,** 35-50.

Frets, E., Tommasi, A., Garrido, C. J., Padrón-Navarta, J. A., Amri, I., Targuisti, K. 2012. Deformation processes and rheology of pyroxenites under lithospheric mantle conditions. *Journal of Structural Geology*, **39,** 138-157.

Godel, B., Seat, Z., Maier, W. D. & Barnes, S.-J. 2011. The Nebo-Babel Ni-Cu-PGE sulfide deposit (West Musgrave block, Australia): Pt. 2. Constraints on parental magma and processes, with implications for mineral exploration. *Economic Geology*, **106,** 557-584.

Gouedji, G. E. F. 2014. *Les séquences mafiques-ultramafiques de Samapleu et leurs minéralisations en Ni-Cu-EGP: un dyke du complexe lité Yacouba ; craton archéen de Man. Ouest Côte d'Ivoire*. PhD thesis en co-tutelle Université Franche Comté-Besançon France / Université Félix Houphouet Boigny, Abidjan.

Gouedji, F., Picard, C., Coulibaly, Y., Audet, M.-A., Auge, T., Goncalves, P., Paquette, J.-L. & Ouattara, N. 2014. The Samapleu mafic-ultramafic intrusion and its Ni-Cu-PGE mineralization: an Eburnean (2.09 Ga) feeder dyke to the Yacouba Layered Complex (Man Archean craton. Western Ivory Coast). *Bulletin de la Société géologique de France*, **185,** 393-411.

Gouedji, G. E. F., Audet, M.-A., Coulibaly, Y., Picard, C., Ouattara, N. & Bakayoko, B. 2018a. Apport de la minéralogie et de la cristallochimie à la connaissance des conditions de mise en place de l'intrusion mafique-ultramafique à Ni-Cu-EGP de Samapleu (complexe lité Yacouba, ouest de la Côte d'Ivoire). *Revue africain et malgache de recherches scientifiques*, **06 (01),** 49-67.

Gouedji, G. E. F., Picard, C., Audet, M.-A., Coulibaly, Y., Deschamps, Q. & Bakayoko, B. 2018b. Les chromitites du complexe lité Yacouba (régions de Biankouma et de Sipilou, Ouest de la Côte d'Ivoire) : pétrographie et cristallochimie. *Revue Ivoirienne des Sciences et Technologie*, **31,** 161-185.

Holland, T. J. B. & Powell, R. 1998. An internally-consistent thermodynamic dataset for phases of petrologist interest. *Journal of Metamorphic Geology*, **16,** 309-343.

Hui, H., Niu, Y., Zhidan, Z., Huixin, H. & Dicheng, Z. 2011. On the enigma of Nb-Ta and Zr-Hf fractionation-A critical review. *Journal of Earth Science*, **22, 1,** 52-66.

Irvine, T. N. 1975. Crystallization sequences in the Muskox intrusions and other layered intrusions. Origin of the chromitite layers and similar deposits of the other magmatic ores. *Geochimica et Cosmochemica Acta*, **39,** 991-1020.

Irvine, T. N. 1977. Crystallization sequences in the Muskox intrusions and other stratiform intrusions: A new interpretations. *Geology*, **5,** 273-277.

Jochum, K. P., Pfander, J., Snow, J. E. & Hofmann, A. W. 1997. Nb/Ta in mantle and crust. *EOS (Trans. Am. Geophys. Union)*, **78,** 804.

Kelsey, D. E., White, R. W. & Powell, R. 2004. Calculated phase equilibria in K_2O-FeO-MgO-Al_2O_3-SiO_2-H_2O for silica-undersaturated sapphirine-bearing mineral assemblages. *Journal of Metamorphic Geology*, **23,** 217-239.

Kouamelan, A. N. 1996. *Géochronologie et géochimie des formations archéennes et protérozoïques de la dorsale de Man en Côte d'Ivoire. Implication pour la transition archéen-protérozoïque.* Thèse de doctorat Université Géosciences de Rennes1, France.

Kouamelan, A. N., Delor, C. & Peucat, J. J. 1997. Geochronological evidence for reworking of Archaean terrains during the Early Proterozoic (2.1 Ga) in the western Côte d'Ivoire (Man Rise - West African Craton). *Precambrian Research*, **86,** 177-199.

Kouamelan, A. N., Djro, S. C., Allialy, M. E., Paquette, J.-L. & Peucat, J. J. 2015. The oldest rock of Ivory Coast. *Journal of African Earth Sciences*, **103,** 65-70.

Kouamelan, A. N., Kouassi, S. A., Djro, S. C., Paquette, J.-L. & Peucat, J. J. 2018. The Logoualé Band: A large Archean crustal block in the Kenema-Man domain (Man-Leo rise. West African Craton) remobilized during Eburnean orogeny (2.05 Ga). *Journal of African Earth Sciences*, **148,** 6-13.

Kretz, R. 1983. Symbols for rock-forming minerals. *American Mineralogist Mineral*, **68,** 277 - 279.

Lassiter, J. C. & DePaolo, D. J. 1997. Plume/lithosphere interaction in the generation of continental and oceanic flood basalts: Chemical and isotopic constraints, *in* Mahoney, J. J. & Coffin, M. F., eds. Large igneous provinces: Continental, oceanic, and planetary flood volcanism: *American Geophysical Union*, **100,** 335-356.

Lompo, M. 2009. Geodynamic evolution of the 2.25-2.0 Ga Palaeoproterozoic magmatic rocks in the Man-Leo shield of the West African craton. A model of subsidence of an oceanic plateau. *Geological Society London*, **323,** 231-254.

Lompo, M. 2010. Paleoproterozoic structural evolution of the Man-Leo shield (West Africa). Key structures for vertical to transcurrent tectonics. *Journal of African Earth Sciences,* **58,** 19-36.

Luo, W., Zhang, Z., Santosh, M., Hou, T., Huang, H., Zhu, J., Wang, X. & Fu, X. 2014. Petrology and geochemistry of Permian mafic–ultramafic intrusions in the Emeishan large igneous province, SW China: Insight into the ore potential. *Ore Geology Reviews*, **56,** 258-275.

Newton, R. C. & Haselton, H. T. 1981. Thermodynamics of the Garnet - Plagioclase - Al_2SiO_5 - Quartz Geobarometer. *Thermodynamics of Minerals and Melts*, **1,** 131-147.

Ouattara, N. 1998. *Pétrologie, géochimie et métallogénie des sulfures et des éléments du groupe du platine des ultrabasites de Côte d'Ivoire : Signification géodynamique et implications sur les processus de croissance crustale à l'Archéen et au Paléoprotérozoïque.* Thèse de doctorat, Université d'Orléans, France.

Peucat, J. J., Capdevila, R., Drareni, A., Mahdjoub, Y. & Kahoui, M. 2005. The Eglab massif in the West African Craton (Algeria). An original segment of the Eburnean orogenic belt: petrology. geochemistry and geochronology. *Precambrian Research*, **136,** 309-352.

Pitra, P., Kouamelan, A. N., Ballevre, M. & Peucat, J. J. 2010. Palaeoproterozoic high pressure granulite overprint of the Archean continental crust: evidence for homogeneous crustal thickening (Man Rise. Ivory Coast). *Journal of Metamorphic Geology*, **28,** 41-58.

Pronost, J. 2005. *Effets de la contamination continentale et des interactions fluides-roches sur le platreef, complexe igné du Bushveld. Afrique du Sud.* Thèse de doctorat. Université Clermont-Ferrand II - Blaise Pascal, France.

Puffer, J. H. 2001. Contrasting high field strength element contents of continental flood basalts from plume versus reactivated-arc sources. *Geology*, **29,** 675-678.

Rudnick, R. L. & Gao, S. 2004. Composition of the continental crust. *Treatrise on Geochemistry*, **3,** 1-64.

Sama Nickel-CI. 2014. Rapport d'activités pour la période du 1er janvier au 31 décembre 2014.

Sanghoon, K., Sung, W. K. & Santosh, M. 2012. Multiple generations of mafic–ultramafic rocks from the Hongseong suture zone. Western South Korea: Implications for the geodynamic evolution of NE Asia. *Lithos*, **160-161,** 68-83.

Sappin, A.-A., Constantin, M. & Clark, T. 2006. Modèle métallogénique des principaux indices de Ni-Cu±EGP du Domaine de Portneuf-Mauricie. *Ressources naturelle et faune*, 1-10.

Schärer, U. & Labrousse, L. 2003. Dating the exhumation of UHP rocks and associated crustal melting in the Norwegian Caledonides. *Contribution to Mineralogy and Petrology*, **144**, 758-770.

Schwartz, S., Guillot, S., Tricart, P., Bernet, M., Jourdan, S., Dumont, T. & Montagnac, G. 2009. Source tracing of detrital serpentinite in the Oligocene molasse deposits from the western Alps (Barrême basin): implications for relief formation in the internal zone. *Cambridge University Geological Magazine*, 1-16.

Sinigoi, S., Quick, J. E., Clemens-Knott, D., Mayer, A., Demarchi, G., Mazzucchelli, M., Negrini, L. & Rivalenti, G. 1994. Chemical evolution of a large mafic intrusion in the lower crust, Ivrea-Verbano Zone, northern Italy. *Journal of Geophysical Research*, **99, 11,** 21575-21590.

Tajčmanová, L., Connolly, J. A. D. & Cesare, B. 2009. A thermodynamic model for titanium and ferric iron solution in biotite. *Journal of Metamorphic Geology*, **27, 2,** 153 - 165.

Thiéblemont, D., Delor, C., Cocherie, A., Lafon, J. M., Goujou, J. C., Balde, A., Bah, M., Sane, H. & Fanning, C. M. 2001. A 3.5 Ga granite / gneiss basement in Guinea: further evidence for early Archean accretion within the West African craton. *Precambrian Research*, **108,** 179-194.

Thiéblemont, D., Goujou, J. C., Egal, E., Cocherie, A., Delor, C., Lafon, J. M. & Fanning, C. M. 2004. Archaean evolution of the Leo Rise and its Eburnean reworking. *Journal of African Earth Sciences*, **39,** 97-104.

Vry, J. K. & Baker, J. A. 2006. LA-MC-ICPMS Pb-Pb dating of rutile from slow cooled granulites: confirmation of the high closure temperature for Pb diffusion in rutile. *Geochimica et Cosmochimica*, Acta **70:** 1807-1820.

White, R. W., Powell, R. & Holland, T. J. B. 2007. Progress relating to calculation of partial melting equilibria for metapelites. *Journal of metamorphic geology*, **25, 5,** 511-527.

Whitney, D. L. & Evans, B. W. 2010. Abbreviations for names of rock-forming minerals. *American Mineralogist*, **95, 1,** 185-187.

Wooden, J. L., Czamanske, G. K., Fedorenko, V. A., Arndt, N. T., Chauvel, C., Bouse, R. M., King, B.-S. W., Knight, R. J. & Siems, D. F. 1993. Isotopic and trace element constraints on mantle and crustal contributions to Siberian continental flood basalts, Noril'sk area, Siberia. *Geochimica et Cosmochimica Acta*, **57,** 3677-3704.

Zack, T., Stockli, D. F., Luvizotto, G. L., Barth, M. G., Belousova, E., Wolfe, M. R. & Hinton, R. W. 2011. In situ U–Pb rutile dating by LA-ICP-MS: ^{208}Pb correction and prospects for geological applications. *Contributions to Mineralogy and Petrology*, **162**, 515–530.

Zhao, J.-X. & McCulloch, M. T. 1993. Melting of a subduction-modified continental lithospheric mantle: Evidence from Late proterozoic mafic dike swarms in central Australia. *Geology*, **21,** 463-466.

Zhao, J. H. & Zhou, M. F. 2006. Neoproterozoic mafic intrusions in the Panzhihua district. SW China: implications for interaction between subducted slab and mantle wedge. *Geochimica et Cosmochimica Acta*, **70,** A740-A1740.

Zhou, M.-F., Arndt, N. T., Malpas, J., Wang, C. Y. & Kennedy, A. K. 2008. Two magma series and associated ore deposit types in the Permian Emeishan large igneous province, SW China. *Lithos*, **103,** 352-368.

Legends of the figures

Fig. 1. Schematic geological map of the study area. (a) West African shield (adapted from fig. 1a, in Berger *et al.* 2013); (b) Man craton in western Ivory Coast (adapted from fig. 2, in Pitra *et al.* 2010); window shows the Sipilou-Biankouma area and the Yacouba layered complex (in Gouedji *et al.* 2014).

Fig. 2. Geological map showing the distribution of The Yacouba layered complex members (in Gouedji *et al.* 2014).

Fig. 3. Photomacrographs and photomicrographs of various mafic and ultramafic sequences of the Samapleu intrusion. (a) Lherzolite weakly serpentinized with a banded structure showing serpentinization olivines, (b) Mesocumulate serpentinized lherzolite (olivine cumulus), (c) Core box indicating chromitite and spinel webstérite (in Gouedji *et al.* 2018), (d) Chromitite with interstitial chromite forming a net texture around pyroxenes (in Gouedji *et al.* 2018),
(e) Macroscopic webstérite, (f) Bronzite and diopside cumulus with spinel exsolution in diopside, (g) Macroscopic gabbronorite, (h) Mesocumulate gabbronorite.
Di, Diopside; Lz, Lizardite; Brz, Bronzite; Prg, Pargasite; Mag, Magnetite; Sulf, Sulfite; Lhz, Lherzolite; Web, Websterite; Spinel websterite, Sp web; Chr, Chromite ; Px, Pyroxene; Sp exs, Spinel exsolution; Byt, Bytownite (Kretz 1983 ; Holland & Powell 1998 ; Whitney & Evans 2010).

Fig. 4. Photomacrograph and photomicrograph of the hybrid lithofacies of the Samapleu intrusion. (a) Macroscopic hybrid lithofacies, (b) Hybrid lithofacies with paragenesis plagioclase, bronzite, sapphirine and biotite.
Pl, plagioclase; Opx = Orthopyroxene; Spr, sapphirine; Bt, biotite; Crd, Cordierite (Newton & Haselton 1981 ; Kretz 1983 ; Holland & Powell 1998 ; Kelsey *et al.* 2004 ; Tajčmanová *et al*. 2009).

Fig. 5. Major element diagrams (SiO_2, Al_2O_3, CaO, Fe_2O_3, TiO_2 and Na_2O) with MgO of Samapleu (E1-SM) sequence cumulates. R^2 = distribution coefficient.

Fig. 6. MORB-normalized Multi-elements patterns for rock samples from Samapleu (E1, SM) intrusion.

Fig. 7. MORB-normalized Multi-elements patterns for hybrid lithofacies from Samapleu (E1) intrusion.

Fig. 8. Chondrite-normalized REE patterns for rock samples from Samapleu (E1, SM) intrusion.

Fig. 9. Chondrite-normalized REE patterns for hybrid lithofacies from Samapleu (E1) intrusion.

Fig. 10. Hybrid lithofacies of the Samapleu intrusion. (a) Photomicrograph of a sample with paragenesis (pyroxene, plagioclase, garnet and sapphirine associated with spinel) showing symplectite texture. (b) Photomicrograph of a sample showing orthopyroxene present in the matrix in the form of large euhedral crystals with abundant plagioclase crystals and euhedral biotite. (c) Photomicrograph showing sapphirine observed as a thin moat surrounding spinel. Opx, Orthopyroxene ; Bt, Biotite ; Pl, Plagioclase ; Grt, Garnet ; Sp, Spinel ; Spr, Sapphirine; Crd, Cordierite (Newton & Haselton 1981 ; Kretz 1983 ; Holland & Powell 1998 ; Kelsey *et al.* 2004 ; White *et al.* 2007 ; Tajčmanová *et al*. 2009 ; Whitney & Evans 2010).

Fig. 11. Diagram showing isopleths. (a) P-T path diagram calculated for sample SM24-33 (Extension 1 area), (b) Isopleths of Mg# and Al_2O_3 contents in Opx, (c) Isopleths of Mg# and TiO_2 (mol) contents in biotite, (d) Isopleths of the pyrope and almandine contents in garnet.

Fig. 12. Chondrite-normalized REE patterns for calculated liquid from Samapleu (E1. SM) intrusion.

Fig. 13. MORB-normalized Multi-elements patterns for calculated liquid from Samapleu (E1. SM) intrusion.

Fig. 14. Sketch of the model of Samapleu intrusion formation modified and adapted from fig. 19, in Godel *et al.* (2011). (a) Under the impingement of a mantle plume at the base of the continental crust, triggers the melting of the shallow mantle (upper mantle) and lead to formation of the basalts composition magmas with a low Ti and high content of MgO; (b) These magmas during their formation and their rise in the continental crust will be assimilated and contaminated by the granulite gneiss of the lower crust (enrichment in Ba. Rb. Th).

Legends of tables

Table 1. *Mineral parageneses of the ultramafic and mafic units of the Samapleu intrusion.*

Table 2. *Mineral parageneses of the hybrid lithofacies of the Samapleu intrusion.*

Table 3. *Limits of determination and uncertainties : Doses of major elements.*

Table 4. *Limits of determination and uncertainties : Doses of trace elements.*

Table 5. *Solid solution models used in this study.*

Table 6. *Major (wt. %), trace elements (ppm) and REE (ppm) geochemical data for the mafic and ultramafic cumulates at the Samapleu (E1, SM) zone.*

Table 7. *Major (wt. %), trace elements (ppm) and REE (ppm) geochemical data for the hybrid lithofacies at the Samapleu zone.*

Table 8. *Representative analyzes of Opx, biotite and garnet from the SM24 (4) 33 sample of the Samapleu intrusion.*

Table 9. *Composition of the calculated liquids of the Samapleu intrusion (TM = 5%)* .

Table 9 continued. *Composition of the calculated liquids of the Samapleu intrusion (TM = 5%).*

Legends of tables

Lithologies	Sites	Boreholes	Samples	Chr	Ol	Lz	Brz	Hyp	En	Di	Prg	Pl	Sp	Mag	Phl	Op
Ultramafic unit																
Chromitite	SM	S12	S12-63	+						+	+			+		+
	SM	S06	S06-59	+	+		+			+				+		+
	SM	S06	S06-32	+	+		+			+	+			+		
	SM	S12	S12-76	+						+				+		+
	E1	SM24-661614	SM24-273.8	+	+		+			+	+		+		+	
	E1	SM24-661614	SM24-102	+	+		+			+	+		+	+		+
Spinel websterite	SM	SM44-505224	SM445/39.9	+	+		+			+	+		+	+		+
	SM	SM44-505224	SM445/42.4	+	+		+			+	+		+	+	+	+

Table 1.

	E1	SM24-661614	SM24-271			+			+	+		+	+			
	E1	SM24-628651	SM24(b)/197.3			+			+	+		+	+			
Dunite	SM	S06	S06-74	+	+							+				
Lherzolite	E1	SM24-661614	SM24-182	+	+	+		+	+	+		+	+			
	E1	SM24-661614	SM24-83	+	+	+		+	+	+		+	+			
	SM	SM44-450250(b)	SM44b-27.8	+	+	+		+	+	+		+	+			
	SM	SM44-450250a	SM44a-38.8	+	+	+		+	+	+		+	+			+
	SM	S06	S06-135	+		+		+	+			+				+
	SM	S06	S06-83	+		+		+	+			+	+			
Harzburgite	SM	T2/2	T2/2-27	+		+	+					+				
	SM	S06	S06-116	+		+	+			+		+	+			
	SM	S12	S12-64	+		+	+			+		+				+
	SM	S16	S16-30	+		+	+			+		+				+
	SM	SM44-680289	SM44 (3)/110	+	+	+	+			+		+	+			+
Olivine websterite	E1	SM24-661614	SM24-217.5	+		+			+	+		+	+			
	E1	SM24-661614	SM24-118.4	+		+			+	+		+	+			
	E1	SM24-661614	SM24-67.8	+		+			+	+		+				
	SM	SM44-450250(b)	SM44b-20.5	+	+	+			+	+		+				
	SM	SM44-517178	SM44-517/72	+	+	+			+	+		+	+			
	SM	SM44-680289	SM44 (3)/115	+	+	+			+	+		+	+	+		+
	SM	S06	S06-154	+		+			+			+				+
	SM	S12	S12-102b	+		+			+			+				
Websterite	E1	SM24-661614	SM24-156			+			+	+		+				
	E1	SM24-661614	SM24-97			+			+	+						+
	E1	SM24-661614	SM24-67.4	+		+			+	+						+
	SM	SM44-450250(b)	SM44b-44.10			+			+	+		+				
	SM	SM44-450250a	SM44a-91.3			+			+	+	+					
	SM	S2A	S2A-2			+			+	+						+
	SM	SM44-517178	SM44-517/179			+			+	+						
	SM	SM44-525290	SM44-525/83			+			+	+		+		+		
	SM	S41	S41-76			+			+	+		+				+
Plagioclase Websterite	E1	SM24-661614	SM24-266			+			+	+	+			+		
	SM	SM44-450250(b)	SM44b-47.3			+			+	+	+					+
	SM	SM44-450250(b)	SM44b-74.6			+			+	+	+	+				
	SM	SM44-450250(b)	SM44b-95.9			+			+	+	+			+		+
	SM	SM44-517178	SM44-517/65			+			+	+	+					
	SM	SM44-525290	SM44-525/119			+			+	+	+			+		+
	SM	S3A	S3A-40			+			+	+	+					+
	SM	S12	S12-60			+			+	+	+	+				+
Mafic unit																
Gabbronorite	E1	SM24-661614	SM24-251			+			+	+	+					
	E1	SM24-480735	SM24-480/352			+			+	+	+					+
	SM	SM44-450250(b)	SM44b-117.8			+			+	+	+			+		+
	SM	SM44-450250(b)	SM44b-130.1			+			+	+	+					
	SM	SM44-450250(c)	SM44c- 122			+			+	+	+					+
	SM	SM44-450250a	SM44a-103			+			+	+	+			+		+
	SM	S12	S12-62			+			+	+	+					
	SM	S2A	S2A-133			+			+	+	+					
Norite	SM	S12	S12-117			+				+	+					+
	SM	S12	S12-206			+				+	+					
Anorthosite	SM	S2A	S2A-79								+					
	SM	S18	S18-90								+					
	SM	S01	S01-45			+					+					+

* **Definition of abbreviations** : SM, Samapleu Main ; E1, Extension 1 ; Chr, Chromite ; Ol, Olivine ; Lz, Lizardite ; Brz, Bronzite ; Hyp, Hypersthene ; En, Enstatite ; Di, Diopside ; Prg, Pargasite ; Pl, Plagioclase ; Sp, Spinel ; Mag, Magnetite ; Phl, Phlogopite ; Op, Opaque minerals (Newton & Haselton 1981 ; Kretz 1983 ; Holland & Powell 1998 ; Whitney & Evans 2010).

Table 2.

Lithologies Hybrid lithofacies	Site	Boreholes	Samples	Opx	Crd	Pl	Bt	Spr	Amp	Ilm	Sp	Grt	Qz	Sil	Zrn	Rt	Op
	E1	SM24-661614	SM24/281	+	+	+	+		+	+				+	+	+	+
	E1	SM24-661614	SM24/279.5	+	+	+	+		+	+	+			+	+	+	+
	E1	SM24-661614	SM24/291	+	+	+	+	+	+						+	+	+
	E1	SM24-661614	SM24/303.5	+		+	+	+	+				+		+	+	+
	E1	SM24-661614	SM24/309	+		+	+		+	+			+		+	+	+
	E1	SM24-661614	SM24/315	+		+	+		+				+		+	+	+
	E1	SM24-628688	SM24 (4)/33	+	+	+		+			+	+	+		+	+	+
	E1	SM24-628688	SM24 (4)/37	+	+	+	+	+			+	+			+		
	E1	SM24-645670	SM24 (3)/30.7	+	+	+	+	+			+	+			+		+
	E1	SM24-645670	SM24 (3)/48.7	+	+	+	+	+				+			+		

* **Definition of abbreviations** : E1, Extension 1 ; Opx, Orthopyroxene ; Crd, Cordierite ; Pl, Plagioclase ; Bt, Biotite ; Spr, Sapphirine ; Amp, Amphibole ; Ilm, Ilmenite ; Sp, Spinel; Grt, Garnet ; Qz, Quartz ; Sil, Sillimanite ; Zrn, Zircon ; Rt, Rutile ; Op, Opaque minerals (Newton & Haselton 1981 ; Kretz 1983 ; Holland & Powell 1998 ; Kelsey *et al.* 2004 ; White *et al.* 2007 ; Tajčmanová *et al*. 2009 ; Whitney & Evans 2010)

Table 3.

Oxides (%)	>10%	>5%	>1%	>0.5%	>0.1%	>0.05%	>0.01%	>0.005%	** Limits of determination* %
SiO_2	<1%			<10%	**				0.5
TiO_2				<5%		<10%		**	0.001
Al_2O_3	<1%			<10%		**			0.02
Fe_2O_3			<2%		<5%	<15%	**		0.01
MnO			<1%		<5%		<10%	**	0.0005
MgO		<2%	<5%			<10%	**		0.02
CaO		<2%		<5%	<10%	**			0.035
Na_2O		<2%			<15%	**			0.03
K_2O		<2%		<5%	<10%	<15%	**		0.01
P_2O_5			<5%		<10%	**			0.05

*Limits of determination; **Uncertainties

Table 4.

	>50 ppm	>10 ppm	>1 ppm	>0.1 ppm	>0.01 ppm	*Limites détermination (ppm)
As	<5%	<10%	**			1.1
Ba	<5%	<10%	**			1.5
Be	<5%	<10%	**			0.4
Bi		<5%	<10%	**		0.1
Cd		<5%	<15%	**		0.12
Ce		<5%	<10%	**		0.1
Co	<5%	<10%	<15%	**		0.35
Cr	<5%	<10%	**			4
Cs		<5%	<10%	**		0.15
Cu	<5%	<10%	**			4.5
Dy			<5%	<10%	<15%	0.007
Er			<5%	<10%	**	0.003
Eu				<5%	<10%	0.004
Ga		<5%	<8%	**		0.2
Gd				<5%	<10%	0.02
Ge		<5%	<8%	**		0.11
Hf		<5%	<10%	<15%	**	0.03
Ho			<5%	<10%	**	0.001
In			<5%	**		0.1
La			<5%	<10%	**	0.06
Lu				<5%	<10%	0.001
Mo		<5%	<10%	**		0.3
Nb		<5%	<10%	<15%	**	0.06
Nd			<5%	<10%	**	0.03
Ni	<5%	**				4.5
Pb		<5%	<10%	**		0.9
Pr			<5%	<10%	**	0.008
Rb		<5%	<10%	**		0.3
Sb		<5%	<10%	**		0.1
Sm			<5%	<10%	**	0.007
Sn	<5%	<10%	<15%	**		0.4
Sr	<5%	<10%	**			1.4
Ta		<5%	<10%	<15%	**	0.015
Tb				<5%	<10%	0.004
Th		<5%	<10%	<15%	**	0.02
Tm			<5%	<10%	**	0.005
U	<5%	<10%		<15%	**	0.03
V	<5%	<10%	**			0.45
W	<5%	<10%	<15%	**		0.2
Y		<5%	**			0.4
Yb			<5%	<10%	**	0.003
Zn	<10%	**				14
Zr	<8%	<15%	**			0.8

*Limits of determination; **Uncertainties

Table 5.

Phases	Solution models labels from perple_X	labels in Fig. 11	References
Biotite	Bt(TCC)	Bt	Tajčmanová *et al.* (2009)
Chlorite	Chl(HP)	Chl	Holland & Powell (1998)
Cordierite	hCrd	Crd	Holland & Powell (1998)
Garnet	Grt(WPH)	Grt	White *et al.* (2007)
Melt	Melt(HP)	L	White *et al.* (2007)
Orthopyroxene	Opx(HP)	Opx	Holland & Powell (1998)
Plagioclase	Pl(h)	Pl	Newton & Haselton (1981)
Sapphirine	Sapp(KWP)	Spr	Kelsey *et al.* (2004)
Spinel	Sp(HP)	Sp	Holland & Powell (1998)

Table 6.

Lithologies	Lherzolite				Olivine websterite									Websterite		
Sites	SM	E1	E1	E1	SM	E1	E1	E1	E1	E1	E1	E1	E1	SM	SM	SM
Samples	SM44(b) / 27.3	SM24 /83	SM24 /173.8	SM24 /182	SM44(b) / 20.4	SM24 /208.5	SM24 /108.2	SM24 /239	SM24 /76.7	SM24 /67.8	SM24 /118.4	SM24 /197.6	SM24 /217.5	SM44(b) / 62.4	SM44(b) / 93.6	SM44(b) / 105.75
SiO_2 (wt%)	41.34	38.62	38.16	38.94	40.21	45.14	43.63	43.73	45.46	42.87	41.46	44.99	46.31	48.4	50.75	50.91
TiO_2	0.05	0.23	0.11	0.12	0.11	0.12	0.2	0.12	0.19	0.13	0.18	0.15	0.13	0.23	0.32	0.24
Al_2O_3	3.25	3.34	2.22	2.65	9.03	7.27	6.68	9.62	3.9	3.33	5.13	8.64	6.47	9.44	7.37	6.51
Fe_2O_3	15.9	15.87	14.82	16.21	15.21	16.9	15.68	14.75	15.11	19.1	16.75	14.42	15.01	13.68	13.26	14.44
MnO	0.2	0.26	0.21	0.24	0.18	0.2	0.19	0.19	0.32	0.32	0.2	0.19	0.19	0.21	0.22	0.25
MgO	30.48	30.02	31.27	32.52	26.41	26.03	27.33	24.67	26.37	27.03	28.53	24.87	26.52	20.04	19.42	21.61
CaO	1.98	3.24	3	3.1	4.81	3.18	3.86	5.33	7.77	4.17	4.96	5.67	3.32	6.1	6.49	4.67
Na_2O	0.31	0.07	0.06	0.2	0.63	0.12	0.28	0.36	0.14	0.34	0.21	0.31	0.36	0.73	0.65	0.32
K_2O	0.1	bd	bd	0.05	0.09	0.01	0.05	0.06	bd	0.08	0.03	0.04	0.05	0.07	0.43	0.07
P_2O_5	bd	bd	bd	bd	bd	bd	bd	bd	bd	bd	bd	bd	bd	bd	bd	bd
LOI	5.1	6.48	7.89	4.65	0.73	-0.22	-0.08	1.14	1.19	1.03	0.59	0.4	0.25	0.13	-0.07	-0.37
Total	98.69	98.12	97.74	98.67	97.41	98.75	97.81	99.95	100.45	98.38	98.04	99.68	98.6	99.02	98.83	98.65
Ni (ppm)	2374	2554	1919	2094	1539	1776	1649	2009	1356	1378	2661	1299	1325	715.1	985.3	695.2
Co	152.8	173.1	139.8	168.1	145.7	131.7	134.8	143	114.7	119.8	181.2	119	124.3	81.22	84.26	87.16
Cr	1233	6890	7241	6927	8681	9600	9428	5401	4125	7147	3603	6278	3481	2197	2172	2322
Cu	678.3	510.4	333	233.6	272.4	688.5	284.9	651.4	648.8	582.4	940.9	369.1	519.1	667.5	537.3	433.9
Sc	12.91	na	na	na	14.36	na	na	na	na	na	na	na	na	33.08	43.12	41.48
As	bd	bd	1.82	5.19	bd	bd	1.56	bd	bd	bd	bd	bd	bd	bd	bd	bd
Ba	63.31	4.21	7.53	14.08	38.64	1.75	11.25	3.4	15.05	20.02	6.74	3.82	4.6	10.1	273.3	17.76
Be	bd	bd	1.98	1.65	bd	bd	0.69	bd	bd	bd	bd	bd	bd	bd	bd	bd
Bi	0.16	0.42	0.58	0.46	bd	0.4	0.31	0.53	1.91	1.23	1.03	0.38	0.4	0.11	bd	0.37
Cd	bd	0.21	0.59	0.48	bd	0.15	bd	0.16	0.36	0.38	0.27	0.15	0.17	0.24	0.25	0.2
Cs	bd	bd	bd	bd	bd	bd	bd	bd	bd	bd	bd	bd	bd	bd	0.3	bd
Ga	2.98	5.28	3.44	4.13	9.24	10.8	7.64	9.03	5.99	6.89	5.52	9.06	7.11	9	9.26	8.55
Ge	1.07	1.18	1.15	1.02	1.07	1.68	1.26	1.33	2.35	1.51	1.34	1.42	1.57	1.77	1.79	1.84
Hf	0.1	0.15	0.23	0.16	0.15	0.15	0.23	0.17	0.33	0.43	0.25	0.27	0.19	0.18	0.75	0.3
In	bd	bd	bd	bd	bd	bd	bd	bd	bd	bd	bd	bd	bd	bd	bd	bd
Mo	bd	0.43	bd	bd	bd	0.35	bd	0.33	0.57	1.94	bd	bd	bd	bd	0.64	1.05
Nb	0.24	0	0	0.2	0.19	0.18	0	0.45	0.34	0.58	0.3	0.39	0.53	0.28	0.9	0.9
Pb	bd	0.93	25.48	23.03	bd	bd	18.36	bd	57.27	1.82	1.14	1.24	5.87	bd	2.37	1.3
Rb	1.52	bd	0.94	1.88	1.19	bd	1.1	1.02	bd	1.56	0.37	0.46	0.6	0.43	12.83	0.72
Sb	bd	bd	0.29	bd	bd	bd	0.29	bd	bd	bd	bd	bd	bd	bd	bd	bd
Sn	bd	0.46	1.69	1.52	bd	0.41	2.1	0.67	1.02	2.55	0.73	0.71	0.6	bd	bd	bd
Sr	18.22	6.71	10.26	16.55	41.92	4.02	17.14	7.33	34.31	17.55	14.81	8.98	8.12	64.22	48.4	41.81
Ta	0.03	bd	bd	0.05	0.02	0.02	bd	0.07	0.16	0.08	0.04	0.08	0.05	0.02	0.12	0.13
Th	bd	bd	bd	0.34	bd	bd	bd	bd	0.05	0.57	0.08	0.04	0.03	bd	0.61	0.19
U	bd	bd	bd	0.09	bd	bd	bd	bd	bd	0.17	bd	bd	bd	bd	0.15	0.06
V	33.5	100.7	68.5	79.42	99.44	127.9	140.6	98	81.39	91.6	84.64	107.1	91.16	120.5	169.1	161.4
W	bd	bd	0.24	0.51	bd	bd	0.31	bd	10.62	1	bd	bd	bd	bd	bd	bd
Y	1.1	3.41	2.8	2.77	1.81	2.07	3.54	3.09	4.74	3.22	4.38	4.48	3.15	4.69	7.86	6.61
Zn	61.29	128.5	263.4	236.2	168.6	161.8	217.4	111.2	164.1	173.9	73.55	117.5	93.97	89.44	99.61	99.43
Zr	3.86	2.36	6.75	7.22	4.57	4.75	7.12	5	10.73	15.52	9.27	8.4	6.56	4.35	21.8	8.18
La	0.55	0.1	0.71	1.37	1.05	0.43	0.65	0.63	1.45	1.48	1.22	1.04	0.79	0.55	5.16	2.16
Ce	1.4	0.55	1.51	2.15	1.99	1.04	1.42	1.69	3.51	2.69	3	2.87	1.91	2.18	11.44	5.81
Pr	0.18	0.15	0.24	0.28	0.22	0.14	0.24	0.24	0.5	0.35	0.41	0.41	0.25	0.35	1.42	0.84
Nd	0.72	0.99	1.01	1.04	0.86	0.64	1.09	1.04	2.38	1.45	1.9	1.78	1.09	1.63	5.46	3.73
Sm	0.16	0.39	0.31	0.28	0.22	0.2	0.39	0.3	0.71	0.38	0.52	0.51	0.3	0.47	1.18	0.93
Eu	0.05	0.12	0.09	0.1	0.11	0.04	0.06	0.13	0.17	0.1	0.11	0.17	0.07	0.21	0.33	0.21
Gd	0.17	0.54	0.34	0.31	0.24	0.25	0.5	0.39	0.83	0.44	0.64	0.6	0.38	0.58	1.18	0.88
Tb	0.03	0.09	0.05	0.06	0.04	0.05	0.08	0.07	0.13	0.08	0.11	0.11	0.07	0.1	0.2	0.16
Dy	0.17	0.62	0.4	0.34	0.28	0.33	0.6	0.48	0.8	0.51	0.73	0.72	0.49	0.75	1.32	1.05
Ho	0.04	0.13	0.09	0.08	0.06	0.07	0.12	0.1	0.16	0.11	0.16	0.15	0.11	0.17	0.28	0.23
Er	0.12	0.37	0.24	0.22	0.19	0.23	0.38	0.32	0.45	0.35	0.43	0.45	0.32	0.51	0.84	0.67
Tm	0.02	0.06	0.04	0.03	0.03	0.04	0.05	0.05	0.07	0.05	0.07	0.07	0.06	0.08	0.14	0.12
Yb	0.15	0.38	0.27	0.25	0.22	0.29	0.34	0.37	0.45	0.4	0.47	0.53	0.4	0.57	0.95	0.84
Lu	0.02	0.06	0.04	0.04	0.04	0.05	0.06	0.06	0.07	0.06	0.08	0.08	0.07	0.09	0.15	0.14
(La/Sm)n	2.11	0.16	1.46	3.1	3.03	1.4	1.05	1.31	1.27	2.45	1.48	1.3	1.66	0.73	2.74	1.46
(La/Yb)n	2.44	0.17	1.77	3.67	3.3	1.01	1.28	1.13	2.19	2.47	1.74	1.33	1.33	0.65	3.67	1.74
(Dy/Yb)n	0.74	1.07	0.96	0.87	0.85	0.73	1.14	0.83	1.16	0.82	1	0.88	0.79	0.86	0.91	0.82

* bd : below detection; † na : not analysed**Table 6 continued.**

Lithologies	Websterite						Plagioclase websterite				Gabbronorite			
Sites	E1	E1	E1	E1	E1	E1	SM	E1	E1	E1	SM	SM	E1	E1
Samples	SM24 /139	SM24 /156.5	SM24 /67.4	SM24 /97.8	SM24 /186	SM24 /274.8	SM44(b) /126	SM24 / 257.4	SM24 / 260.3	SM24 /266.3	SM44(b) / 134.2	SM44(b) / 142.3	SM24 /251	SM24 / 254.5
SiO_2 (wt%)	46.47	50.84	48.6	46.91	43.47	48.68	45.38	46.05	45.66	49.67	47.15	47.77	46.67	47.39
TiO_2	0.16	0.19	0.11	0.18	0.18	0.16	0.23	0.12	0.19	0.16	0.19	0.2	0.22	0.22
Al_2O_3	7.38	5.72	3.33	7.17	7.86	7.9	11.37	6.42	9.48	7.05	18.34	15.72	19.2	19.66
Fe_2O_3	16.22	12.35	17.06	15.05	13.75	16.39	12.42	21.9	13.14	14.59	6.64	7.5	7.5	8.31
MnO	0.22	0.24	0.34	0.2	0.15	0.25	0.17	0.28	0.17	0.22	0.13	0.15	0.13	0.13
MgO	24.34	25.01	23.79	25.14	23.78	24.25	19.69	20.16	22.68	23.97	11.37	12.91	10.59	11.53
CaO	3.25	5.57	4.39	3.93	4.77	0.75	7.68	1.88	3.82	2.87	14.15	13.86	12.13	9.87
Na_2O	0.1	0.3	0.27	0.29	0.37	0.21	1.07	0.22	0.15	0.28	0.95	0.84	1.58	1.29
K_2O	bd	0.05	0.07	0.03	0.06	0.11	0.1	0.03	1.65	0.11	0.01	0.01	0.15	0.12
P_2O_5	bd	bd	bd	bd	bd	0.05	bd	bd	bd	bd	bd	bd	bd	bd

LOI	-0.2	-0.03	2.25	0.05	3.64	-0.07	0.63	0.33	1.02	0.43	0.15	0.37	1.03	0.8
Total	97.94	100.23	100.2	98.95	98.02	98.68	98.74	97.38	97.95	99.35	99.06	99.33	99.21	99.32
Ni (ppm)	1612	592.6	3020	1108	1288	1464	693.3	2727	1029	1057	217.8	238.7	252.4	279.6
Co	113.1	63.75	155.7	108.9	112.5	105.6	88.42	181	94.3	79.9	40.46	45.84	42.19	49.55
Cr	8648	4092	5171	540.7	8689	6980	1797	5390	6776	3414	858.4	955.5	695.6	756.9
Cu	530	75.95	1954	976.1	949.2	1006	92.98	2355	1227	1004	105.8	141.7	46.75	87.75
Sc	na	na	na	na	na	na	34.7	23.06	16.23	na	38.52	43.86	na	29.66
As	bd	bd	1.19	bd	3.6	bd	bd	bd	bd	bd	bd	bd	1.2	bd
Ba	10.49	7.81	21.1	6.96	9.9	985.6	6.69	36.69	1166	149	bd	1.6	81.36	235.6
Be	bd	bd	0.41	bd	0.78	bd	bd	bd	bd	0.52	bd	bd	bd	bd
Bi	0.23	0.16	1.65	0.51	0.55	0.18	bd	0.34	0.78	1.06	bd	bd	0.63	0.68
Cd	0.34	0.39	0.57	0.24	0.14	0.27	bd	0.29	0.3	0.32	bd	bd	0.29	0.37
Cs	bd	bd	bd	bd	bd	0.66	bd	bd	13.14	0.23	bd	bd	bd	bd
Ga	12.22	6.32	11.21	6.11	8.89	11.6	8.5	14.94	9.07	9.5	12.96	11.31	13.96	13.64
Ge	1.53	1.55	1.88	1.42	1.49	1.79	1.52	1.78	1.62	1.75	1.35	1.59	1.4	1.18
Hf	0.14	0.23	0.2	0.34	0.36	0.22	0.1	0.17	0.36	0.51	0.11	0.12	0.2	0.15
In	bd	bd	0.11	bd	bd	bd	bd	0.09	bd	bd	bd	bd	bd	bd
Mo	0.34	bd	9.03	0.33	0.63	6.27	bd	90.67	1.82	3.46	bd	bd	0.35	bd
Nb	0.11	0.33	0.54	0.39	0.33	1.03	0.16	bd	0.58	0.5	0.14	0.15	0.37	0.37
Pb	bd	1.71	6.73	52.87	49.16	37.81	bd	1.24	0.94	35.84	bd	bd	4.88	6
Rb	0.71	0.54	1.17	0.57	1.59	7.59	0.61	0.85	102.3	3.02	bd	bd	4.26	1.4
Sb	bd	bd	bd	bd	0.21	bd	bd	bd	bd	bd	bd	bd	bd	bd
Sn	0.53	1.03	3.37	0.44	1.36	0.74	0.56	bd	0.81	0.81	bd	bd	0.85	bd
Sr	7.49	24.43	13.67	7.73	14.03	30.27	18.37	51.02	23.03	27.35	114.2	92.27	388.8	433.6
Ta	0.02	0.03	0.08	0.04	0.04	0.19	bd	0.02	0.07	0.09	0.13	0.02	0.02	0.02
Th	bd	bd	0.39	0.13	0.33	0.08	bd	0.05	0.22	0.18	bd	bd	bd	bd
U	bd	bd	0.1	0.03	0.11	bd	bd	bd	0.07	0.06	bd	bd	bd	bd
V	132.5	120	78.47	68.84	136	124.9	145.9	160.7	134.2	109	127.9	141.4	118	106.9
W	bd	bd	0.46	bd	0.57	bd	bd	bd	bd	bd	bd	bd	bd	bd
Y	2.34	4.29	3.96	3.48	3.81	3.09	3.39	2.52	4.43	3.69	4.51	4.8	5.15	4.35
Zn	205.8	97.73	129.9	60.72	213	257.2	81.24	241.9	170.2	100	38.42	44.03	54.84	59.46
Zr	3.68	6.94	7.06	10.41	12.86	8.66	2.68	4.55	12.81	18.33	2.25	2.48	5.42	3.47
La	0.24	0.69	1.51	1.06	1.24	1.63	0.36	0.93	2.24	2.54	0.27	0.27	1.04	1.12
Ce	0.8	2.24	3.6	2.19	2.63	2.64	1.23	1.72	6.43	4.5	0.93	1	2.18	1.95
Pr	0.13	0.34	0.5	0.29	0.37	0.28	0.18	0.2	0.8	0.52	0.18	0.19	0.32	0.25
Nd	0.67	1.5	2.06	1.35	1.65	1.07	0.84	0.78	3.04	2.09	0.98	1.06	1.59	1.18
Sm	0.21	0.41	0.56	0.38	0.49	0.27	0.24	0.19	0.65	0.48	0.4	0.39	0.49	0.38
Eu	0.09	0.24	0.15	0.09	0.1	0.07	0.37	0.08	0.16	0.14	0.21	0.2	0.29	0.2
Gd	0.27	0.54	0.59	0.47	0.5	0.32	0.36	0.26	0.68	0.51	0.57	0.6	0.67	0.56
Tb	0.05	0.1	0.1	0.09	0.09	0.06	0.07	0.05	0.12	0.09	0.11	0.11	0.12	0.1
Dy	0.36	0.68	0.64	0.58	0.59	0.45	0.51	0.35	0.74	0.57	0.74	0.81	0.83	0.73
Ho	0.08	0.15	0.13	0.13	0.12	0.11	0.12	0.08	0.16	0.12	0.16	0.17	0.18	0.16
Er	0.25	0.47	0.38	0.36	0.4	0.34	0.37	0.28	0.45	0.39	0.49	0.5	0.52	0.47
Tm	0.04	0.08	0.06	0.06	0.06	0.06	0.06	0.06	0.07	0.07	0.07	0.08	0.08	0.07
Yb	0.33	0.54	0.44	0.41	0.45	0.44	0.45	0.46	0.49	0.47	0.48	0.51	0.57	0.49
Lu	0.06	0.09	0.07	0.07	0.07	0.07	0.07	0.08	0.08	0.08	0.07	0.08	0.09	0.08
(La/Sm)n	0.73	1.04	1.68	1.76	1.61	3.8	0.95	3	2.17	3.32	0.42	0.43	1.34	1.84
(La/Yb)n	0.5	0.86	2.29	1.76	1.87	2.5	0.54	1.36	3.08	3.62	0.38	0.35	1.24	1.52
(Dy/Yb)n	0.72	0.83	0.93	0.93	0.86	0.67	0.73	0.5	0.98	0.78	1	1.03	0.95	0.96

* bd : below detection ; † na : not analysed**Table 7.**

Lithologies	Hybrid lithofacies								
Site	E1	E1	E1	E1	E1	E1	E1	E1	E1
Samples	SM24 /309	SM24 /281	SM24 /279.5	SM24 /291	SM24 /303.5	SM24 (4) /33	SM24 (4) /37	SM24 (3) /30.7	SM24 (3) /48.7
SiO_2 (wt%)	55.85	54.7	54.09	45.52	49.55	49.14	38.88	50.3	43.43
TiO_2	0.07	0.15	0.11	0.14	0.2	0.59	0.51	0.33	1.1
Al_2O_3	23.86	14.46	15.6	25.58	9.99	17.23	32.94	9.58	25.28
Fe_2O_3	3.01	10.17	9.87	8.05	13.7	13.53	8.88	14.29	8.76
MnO	0.05	0.17	0.14	0.12	0.19	0.18	0.1	0.25	0.09
MgO	3.3	13.97	12.62	12.28	21.43	14.44	13.96	22.31	14.15
CaO	8.31	4.19	4.59	5.11	2.03	4.12	3.1	1.92	4.39
Na_2O	4.95	2.71	3.09	2.31	0.78	1.73	1.85	0.59	1.68
K_2O	0.61	0.37	0.3	0.32	0.21	0.14	0.17	0.04	0.11
P_2O_5	bd	bd	bd	bd	bd	bd	0.03	bd	bd
LOI	0.6	0	0.17	0.93	0.47	-0.49	0.2	-0.47	0.03
Total	100.6	100.88	100.57	100.34	98.54	100.6	100.62	99.13	99.02
Ni (ppm)	65.23	135.6	576.5	125.8	920.7	49.45	73.36	228.2	45.79
Co	14.18	29.98	42.83	27.96	53.43	42.09	25.55	53.68	27.24
Cr	45.14	190.6	367.6	64.36	515.1	61.28	60.16	173.2	65.45
Cu	214.9	56.25	714.3	62.9	643.4	22.78	9.87	27.33	29.7
Sc	na	14.41	11.41	na	na	20	9.25	20.2	10.28
As	bd	bd	bd	bd	bd	bd	bd	bd	bd
Ba	408.2	219.6	304	225.1	571.5	112.9	166.6	45.59	158.9
Be	1.95	1.54	1.01	25.7	1.2	0.87	9.5	2.06	7.23
Bi	bd	bd	bd	bd	0.13	bd	bd	bd	0.27

Cd	bd	0.19	0.2	0.2	0.74	bd	0.14	0.16	0.43
Cs	bd	0.12	0.1	bd	0.79	0.1	bd	bd	0.08
Ga	23.81	18.51	19.5	44.73	19.9	29.36	66.73	21.61	46.48
Ge	0.77	1.42	1.35	0.94	1.78	1.25	0.8	1.41	0.74
Hf	0.38	1.83	2.39	4.58	1.68	1.77	4.8	2.93	17.55
In	bd	bd	bd	bd	0.11	bd	bd	bd	bd
Mo	1.01	54.2	5.94	9.19	513.5	1.54	2.79	1.27	68.78
Nb	0.4	1.14	0.93	0.21	1.23	5.67	13.09	5.33	27.88
Pb	8.47	4.67	3.89	6.2	32.54	2.55	3.13	0.93	2.53
Rb	3.12	4.17	3.29	3.74	8.34	1.54	1.24	0.56	1.49
Sb	bd	bd	bd	bd	bd	bd	bd	bd	bd
Sn	bd	bd	bd	0.61	0.7	bd	bd	bd	0.88
Sr	528.4	284.9	414.6	266.8	137.1	197.4	189.2	96.66	420.3
Ta	0.04	0.14	0.1	0.03	0.23	0.48	1.29	0.41	2.39
Th	0.35	0.55	0.14	0.17	0.11	0.22	0.42	0.08	1.32
U	0.08	0.28	0.12	0.29	0.07	0.15	0.23	0.1	0.32
V	20.51	74.58	60.63	52.15	138.8	148.9	112.7	132.4	120.2
W	bd	0.39	0.58	bd	0.49	1.49	2	2.47	450.2
Y	1.67	3.66	2.06	3.44	2.55	4.53	2.92	3.68	2.08
Zn	41.42	113.8	109.7	144.6	163.7	153	111.1	183	100.1
Zr	15.02	70.76	94.69	186.3	64.82	63.29	199	118.6	752.7
La	26.55	13.3	8.96	18.18	6.89	9.39	15.86	3.17	15.63
Ce	38.58	20.69	12.1	27.94	9.28	14.81	23.9	5.01	20.45
Pr	3.66	1.97	1.08	2.72	0.85	1.39	2.24	0.48	1.75
Nd	11.05	6.33	3.25	8.71	2.79	4.48	7.09	1.64	5.29
Sm	1.27	0.89	0.43	1.11	0.38	0.66	0.83	0.32	0.62
Eu	1.43	0.73	0.72	0.77	0.26	0.5	0.7	0.18	0.9
Gd	0.68	0.67	0.32	0.74	0.34	0.63	0.55	0.37	0.4
Tb	0.08	0.1	0.05	0.1	0.05	0.1	0.08	0.07	0.06
Dy	0.36	0.58	0.31	0.57	0.37	0.69	0.45	0.52	0.33
Ho	0.06	0.12	0.07	0.12	0.09	0.15	0.09	0.13	0.07
Er	0.16	0.39	0.25	0.37	0.33	0.5	0.33	0.43	0.25
Tm	0.02	0.07	0.05	0.07	0.07	0.09	0.06	0.08	0.05
Yb	0.17	0.52	0.41	0.5	0.56	0.69	0.49	0.66	0.38
Lu	0.03	0.09	0.08	0.09	0.11	0.12	0.1	0.12	0.07
(La/Sm)n	13.17	9.35	13.07	10.27	11.39	9.01	12.07	6.2	15.85
(La/Yb)n	108.37	17.16	14.76	24.68	8.22	9.14	21.71	3.26	28.07
(Dy/Yb)n	1.43	0.72	0.49	0.74	0.42	0.65	0.6	0.51	0.56

* bd : below detection ; † na : not analysed

Table 8.

Lithologie	Hybrid lithofacies									
Site	Extension 1									
Sample	SM24 (4) 33									
Minerals	Opx				Biotite		Garnet			
Analysis	149	150	151	153	158	154	105	120	121	135
SiO_2 (%)	48.96	48.80	48.49	49.81	36.18	35.70	39.39	39.56	39.50	40.00
TiO_2	0.10	0.21	0.16	0.09	3.74	3.28	0.00	0.04	0.01	0.01
Al_2O_3	8.63	9.07	8.56	7.46	16.58	16.33	23.63	22.93	22.87	22.80
Fe_2O_3	2.50	1.31	2.82	1.96	na	na	0.00	0.00	0.30	0.18
FeO	15.71	16.48	15.54	16.29	na	na	21.62	21.85	22.05	22.40
FeO^T	17.96	17.66	18.08	18.06	9.57	9.16	21.62	21.85	22.33	22.50
Cr_2O_3	0.00	0.01	0.02	0.00	0.03	0.01	0.03	0.01	0.00	0.00
MnO	0.19	0.13	0.13	0.12	0.00	0.00	0.55	0.42	0.46	0.54
MgO	23.70	23.39	23.78	24.10	16.33	17.71	12.75	12.60	12.57	12.20
CaO	0.12	0.12	0.11	0.08	0.02	0.05	1.51	1.67	1.68	2.36
Na_2O	0.06	0.01	0.00	0.03	0.16	0.20	0.00	0.06	0.02	0.00
K_2O	0.00	0.01	0.02	0.02	9.49	9.28	0.00	0.00	0.01	0.00
Total	99.97	99.54	99.63	99.97	92.10	91.71	99.48	99.13	99.49	100.00
Si	1.78	1.78	1.77	1.81	2.73	2.70	2.96	2.99	2.98	2.99
Ti	0.00	0.01	0.00	0.00	0.21	0.19	0.00	0.00	0.00	0.00
Al	na	na	na	na	1.47	1.46	2.09	2.04	2.03	2.01
Al^4	0.22	0.22	0.23	0.19	na	na	na	na	na	na
Al^6	0.15	0.17	0.14	0.13	na	na	na	na	na	na
Cr	0.00	0.00	0.00	0.00	0.00	0.00	0.00	0.00	0.00	0.00
Fe^{2+}	0.48	0.50	0.47	0.50	0.60	0.58	1.36	1.38	1.39	1.40
Fe^{3+}	0.07	0.04	0.08	0.05	na	na	0.00	0.00	0.02	0.01
Mn	0.01	0.00	0.00	0.00	0.00	0.00	0.04	0.03	0.03	0.03
Mg	1.28	1.27	1.29	1.31	1.84	2.00	1.43	1.42	1.41	1.37
Ca	0.01	0.01	0.00	0.00	0.00	0.00	0.12	0.14	0.14	0.19
Na	0.00	0.00	0.00	0.00	0.02	0.03	0.00	0.01	0.00	0.00
K	0.00	0.00	0.00	0.00	0.91	0.90	0.00	0.00	0.00	0.00
Total	4.00	4.00	4.00	4.00	7.79	7.85	8.00	8.00	8.00	8.00
Mg#	0.73	0.72	0.73	0.73	0.75	0.78	0.51	0.51	0.50	0.49
% Alm	-	-	-	-	-	-	46.17	46.60	46.90	46.80
% Pyr	-	-	-	-	-	-	48.51	47.90	47.60	45.70
% Sps	-	-	-	-	-	-	1.19	0.90	0.99	1.15
% Grs	-	-	-	-	-	-	4.13	4.57	4.56	6.33

* Oxygen number : 6 O for Opx ; 12 O for garnet; 11 O for biotite ; † na : not analysed

Table 9.

Lithologies	Lherzolite				Olivine Websterite									Websterite		
Site	E1	E1	E1	SM	E1	E1	E1	E1	E1	E1	E1	E1	SM	SM	SM	SM
Samples	SM24 /83	SM24 /173.8	SM24 /182	SM44(b) /27.3	SM24 /208.5	SM24 /108.2	SM24 /239	SM24 /76.7	SM24 /67.8	SM24 /118.4	SM24 /197.6	SM24 /217.5	SM44(b) / 20.4	SM44(b) / 62.4	SM44(b) / 93.6	SM44(b) / 105.75
La (ppm)	1.16	8.5	19.14	6.2	4.7	6.81	7.5	17.73	17.94	14.67	13.51	9.32	10.42	5.16	50.2	21.46
Ce	5.43	14.52	25.64	12.63	8.48	11.24	15.46	33.09	25.3	27.74	29.24	17.14	14.71	15.11	82.94	43.12
Nd	7.2	7.15	9.64	4.73	3.85	6.19	7.12	17.5	10.24	13.24	13.73	7.41	4.47	8.29	28.8	20.9
Sm	1.97	1.51	1.89	0.73	0.81	1.52	1.48	3.76	1.92	2.59	2.87	1.46	0.77	1.6	4.24	3.57
Eu	0.53	0.41	0.61	0.22	0.16	0.22	0.57	0.79	0.46	0.51	0.86	0.32	0.34	0.63	1.03	0.69
Gd	2.43	1.48	1.87	0.65	0.86	1.62	1.56	3.61	1.84	2.62	2.81	1.52	0.7	1.64	3.53	2.83
Tb	0.43	0.22	0.35	0.1	0.16	0.26	0.28	0.57	0.31	0.46	0.48	0.29	0.13	0.3	0.61	0.52
Dy	2.79	1.66	2	0.69	1.01	1.76	1.62	3	1.89	2.62	2.8	1.67	0.77	1.97	3.61	3.06
Ho	0.6	0.39	0.51	0.16	0.24	0.37	0.36	0.64	0.41	0.58	0.61	0.38	0.18	0.46	0.79	0.69
Er	1.8	1.09	1.4	0.52	0.76	1.17	1.14	1.77	1.34	1.63	1.84	1.14	0.56	1.41	2.42	2.05
Tm	0.27	0.17	0.19	0.08	0.11	0.14	0.16	0.24	0.19	0.23	0.26	0.17	0.08	0.21	0.36	0.32
Yb	1.86	1.18	1.58	0.66	0.85	0.97	1.16	1.52	1.4	1.58	1.87	1.24	0.59	1.46	2.5	2.32
Lu	0.3	0.19	0.26	0.11	0.14	0.17	0.17	0.22	0.2	0.23	0.28	0.19	0.1	0.23	0.38	0.36
Ba	25.52	49.67	118.74	341.7	132.01	95.66	107.67	57.1	32.37	14.87	54.58	28.85	208.5	46.01	1392	87.57

Sr	37.82	58.93	122.09	92.58	20.45	83.91	45.9	212.32	108.45	90.3	65.29	48.26	184.5	251.4	153.8	115.9
V	30.75	18.59	32.13	9.57	32.36	37.44	19.3	26.08	18.16	16.74	22.04	20.94	24.59	36.3	68.07	81.62
Cr	662.6	577.4	808.9	118.2	728.7	837.2	258.2	370.3	346.3	174	301.8	204.5	768.5	299	585.1	1154
Ti	5834	2602	3994	1130	2289	3226	3984	3893	3109	2486	3140	2333	1719	3204	4802	3811
Ni	204.6	174	147.7	203.6	290.1	283.4	343.9	410.8	192.1	295.9	194	417.5	325.6	232.9	349.8	256.2
Co	58.88	51.48	52.83	54.18	69.92	72.48	77.41	53.13	56.48	89.44	56.36	65.66	79.36	47.22	52.95	54.46
Zr	17.03	46.26	65.85	25.49	23.22	34.82	26.65	59.21	89.32	51.15	51.83	33.81	21.52	17.79	94.58	35.18
Hf	0.9	1.19	1.11	0.51	0.55	0.82	0.65	1.31	1.8	1	1.13	0.69	0.53	0.58	2.48	1.01
Nb	0	0	2.86	3.06	2.1	0	5.58	4.12	7.38	3.75	5.19	6.35	2.13	2.84	9.92	9.67
Ta	bd	bd	0.6	0.28	0.14	bd	0.62	1.5	0.79	0.34	0.78	0.49	0.18	0.18	0.99	1.06
Th	bd	bd	5.03	bd	bd	bd	bd	0.8	9.83	1.38	0.68	0.47	bd	bd	10.17	3.17
U	bd	bd	1.18	bd	bd	bd	bd	bd	2.71	bd	bd	bd	bd	bd	2.16	0.84
Y	15.61	11.69	16.69	4.49	6.38	10.33	10.36	17.7	11.76	15.54	17.15	10.63	4.95	12.54	21.52	19.47
Cs	bd	bd	bd	bd	bd	bd	bd	bd	bd	bd	bd	bd	bd	bd	3.99	bd
Rb	0	11.6	26.57	16.97	18.76	0	15.58	5.02	6.28	0	9.31	13.89	12.85	4.23	133.01	7.34
(La/Sm)n	0.59	5.63	10.14	8.47	5.77	4.49	5.06	4.71	9.35	5.67	4.71	6.4	13.51	3.22	11.84	6.01
(La/Yb)n	0.62	7.23	12.14	9.33	5.55	7.01	6.48	11.64	12.8	9.31	7.21	7.53	17.63	3.53	20.06	9.27
(Dy/Yb)n	1.51	1.41	1.27	1.04	1.19	1.81	1.4	1.97	1.35	1.66	1.49	1.35	1.3	1.35	1.44	1.32
Nb/Th	bd	bd	0.57	bd	bd	bd	bd	5.15	0.75	2.71	7.63	13.51	bd	bd	0.97	3.05
Th/Yb	bd	bd	3.18	bd	bd	bd	bd	0.53	7.02	0.87	0.36	0.38	bd	bd	4.07	1.37
Zr/Hf	19	38.78	59.14	49.98	42.34	42.7	40.84	45.18	49.74	50.9	45.84	49.05	40.91	30.79	38.08	34.94
Nb/Ta			4.75	10.9	14.78		8.94	2.75	9.29	11.01	6.68	12.96	12.14	15.74	10.06	9.14

* bd : below detection

Table 9 continued.

Lithologies	Websterite						Plagioclase Webstérite				Gabbronorite			
Site	E1	E1	E1	E1	E1	E1	E1	E1	E1	SM	E1	E1	SM	SM
Samples	SM24 /139	SM24 /156.5	SM24 /67.4	SM24 /97.8	SM24 /186	SM24 /274.8	SM24 / 257.4	SM24 / 260.3	SM24 /266.3	SM44(b) /126	SM24 /251	SM24 / 254.5	SM44(b) / 134.2	SM44(b) / 142.3
La (ppm)	2.58	6.55	12.63	10.61	12.3	19.54	10.06	23.69	27.83	3.09	10.7	11.66	2.3	2.41
Ce	6.43	15.77	21.94	16.26	19.45	24.11	14.71	53.06	38.76	8.09	19.2	17.82	6.52	7.59
Nd	4.04	7.37	8.67	7.26	8.81	8.02	5.15	19.22	14.18	3.99	11.24	8.96	5.14	6.15
Sm	0.87	1.37	1.55	1.38	1.76	1.46	0.94	2.93	2.37	0.74	2.62	2.25	1.46	1.62
Eu	0.33	0.7	0.36	0.28	0.32	0.32	0.3	0.58	0.53	0.96	0.96	0.7	0.52	0.56
Gd	0.92	1.49	1.37	1.43	1.52	1.39	1.02	2.54	2.08	0.98	3.14	2.91	1.83	2.18
Tb	0.17	0.27	0.23	0.27	0.26	0.28	0.19	0.45	0.36	0.2	0.58	0.51	0.36	0.42
Dy	1.09	1.72	1.41	1.61	1.64	1.68	1.23	2.45	2.01	1.34	3.6	3.49	2.4	2.92
Ho	0.25	0.4	0.3	0.36	0.35	0.41	0.29	0.54	0.45	0.33	0.8	0.79	0.54	0.64
Er	0.78	1.26	0.92	1.07	1.18	1.29	1.02	1.55	1.41	1.05	2.39	2.39	1.74	1.94
Tm	0.12	0.19	0.14	0.15	0.17	0.19	0.18	0.22	0.21	0.16	0.35	0.34	0.25	0.29
Yb	0.91	1.34	1.02	1.11	1.22	1.42	1.46	1.51	1.52	1.25	2.42	2.31	1.75	1.98
Lu	0.15	0.21	0.15	0.18	0.17	0.21	0.25	0.22	0.23	0.2	0.38	0.36	0.27	0.31
Ba	138.9	37.5	39.8	42.1	52.2	7648	227.1	6831	922.2	23.42	358.5	1019	bd	5.43
Sr	37.4	102.8	45.7	34.02	53.82	121.6	99.6	47.03	53.52	34.73	383.8	398.2	104.6	86.65
V	37.27	34.48	26.02	14.84	34.7	41.57	108.3	84.87	76.15	34.25	95.72	101.9	62.25	81.44
Cr	762.4	528.3	2320	35.94	771.9	626.2	2835	3947	1831	167.4	641.4	807	1112	1129
Ti	1936	2517	1987	2949	2916	3380	2340	3692	3300	3215	5245	5608	3126	3687
Ni	831.5	362.5	455.6	149.6	355.9	361.2	1112.3	416.3	429.5	266.4	170.6	206.7	176.7	180.4
Co	64.05	39.64	87.18	61.87	66.02	58.04	131.9	67.54	57.58	62.04	49.48	62.23	50.25	54.98
Zr	16.96	30.4	27.23	47.09	57.55	42.87	22.56	61.88	90.55	11.05	29.54	19.31	10.43	12.07
Hf	0.47	0.73	0.61	1.15	1.22	0.82	0.66	1.36	1.96	0.35	1.01	0.78	0.5	0.58
Nb	1.28	3.64	5.4	4.34	3.68	11.99	bd	7.11	6.15	1.66	5.2	5.36	1.76	1.94
Ta	0.13	0.25	0.66	0.35	0.31	1.7	0.18	0.65	0.76	0	0.22	0.18	1.25	0.15
Th	bd	bd	6.25	2.22	5.59	1.37	0.71	3.52	2.91	bd	bd	bd	0	0
U	bd	bd	1.34	0.45	1.65	bd	bd	0.97	0.88	bd	bd	bd	bd	bd
Y	7.08	10.77	8.92	9.74	10.61	11.46	8.65	14.56	12.95	9.18	22.29	21.02	15.2	17.79
Cs	bd	bd	bd	bd	bd	10.16	bd	165.6	2.89	bd	bd	bd	bd	bd
Rb	14.05	6.11	6.17	5.83	16.93	98.65	9.58	1125	34.15	5.03	38.85	12.56	0	0
(La/Sm)n	2.98	4.78	8.15	7.71	6.98	13.38	10.75	8.09	11.73	4.16	4.08	5.19	1.57	1.49
(La/Yb)n	2.83	4.9	12.39	9.57	10.1	13.81	6.88	15.73	18.31	2.47	4.43	5.04	1.31	1.22
(Dy/Yb)n	1.19	1.29	1.39	1.45	1.35	1.19	0.84	1.63	1.32	1.08	1.49	1.51	1.37	1.47
Nb/Th	bd	bd	0.86	1.95	0.66	8.75	bd	2.02	2.11	bd	bd	bd	bd	bd
Th/Yb	bd	bd	6.13	2	4.58	0.96	0.49	2.33	1.91	bd	bd	bd	bd	bd
Zr/Hf	36.08	41.64	44.77	41.12	47.25	52.21	34.34	45.45	46.26	31.64	29.32	24.67	20.96	20.87
Nb/Ta	9.95	14.58	8.16	12.24	11.93	7.05	bd	10.86	8.09	bd	23.72	29.24	1.41	13.35

* bd : below detection

List of figures

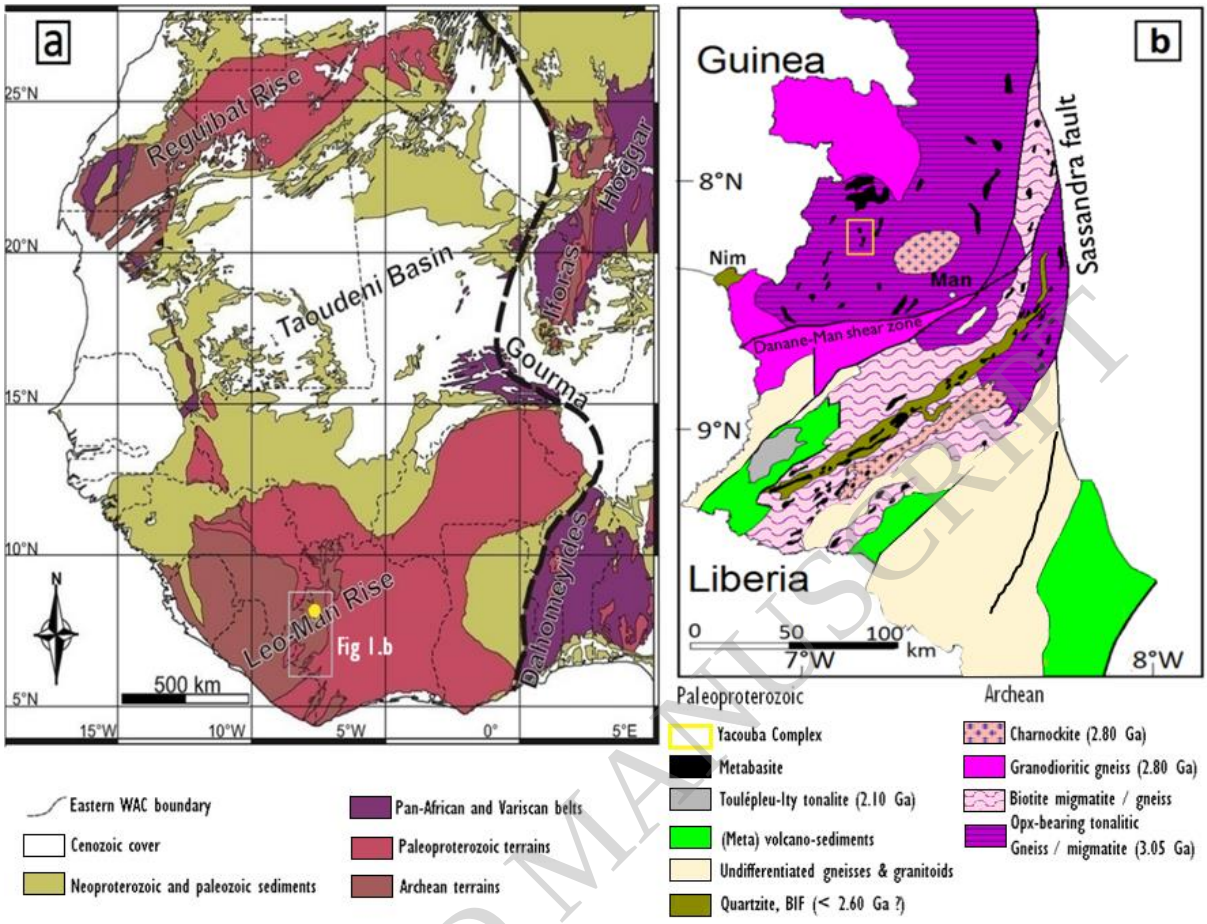

Fig. 1.

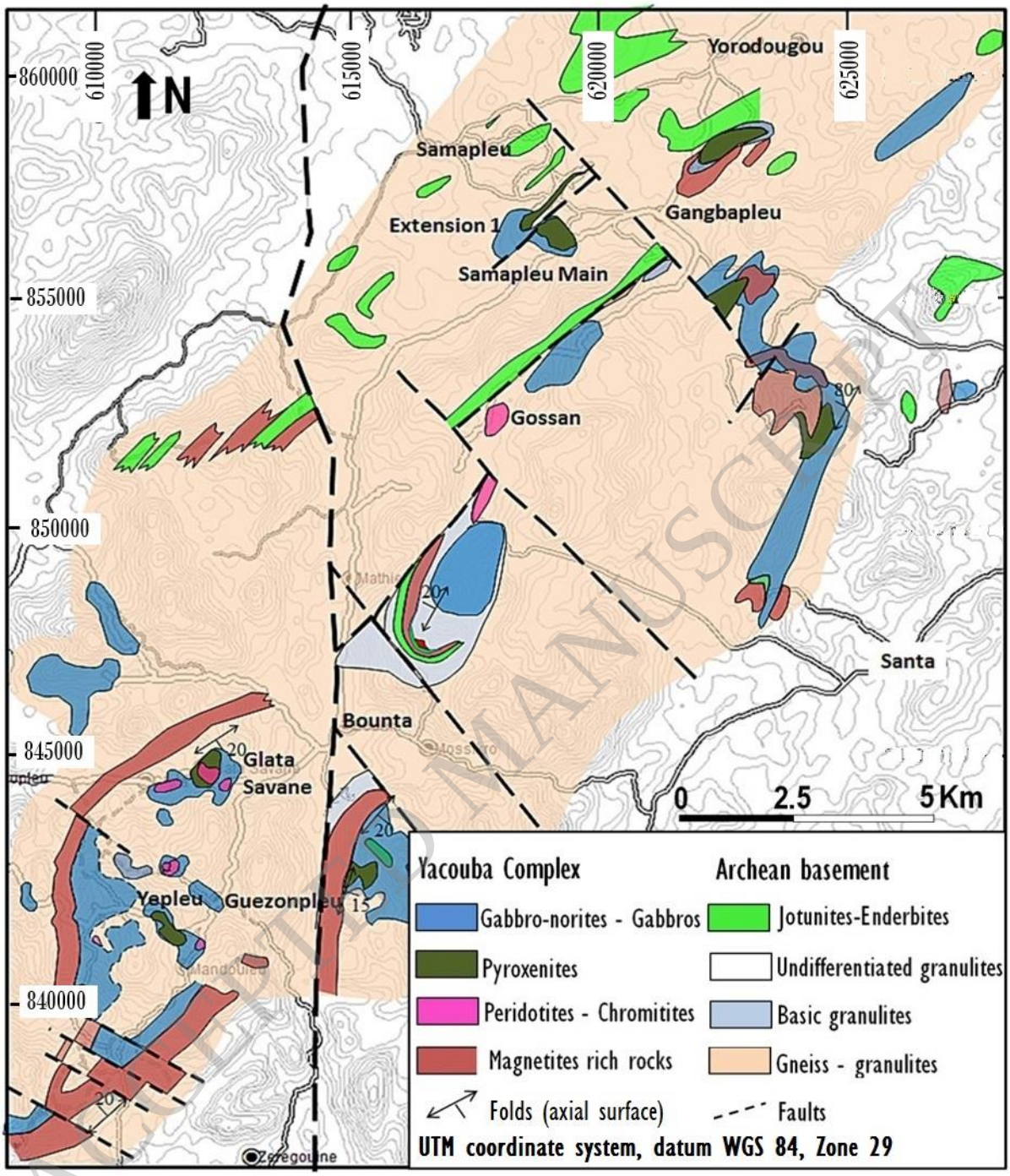

Fig. 2.

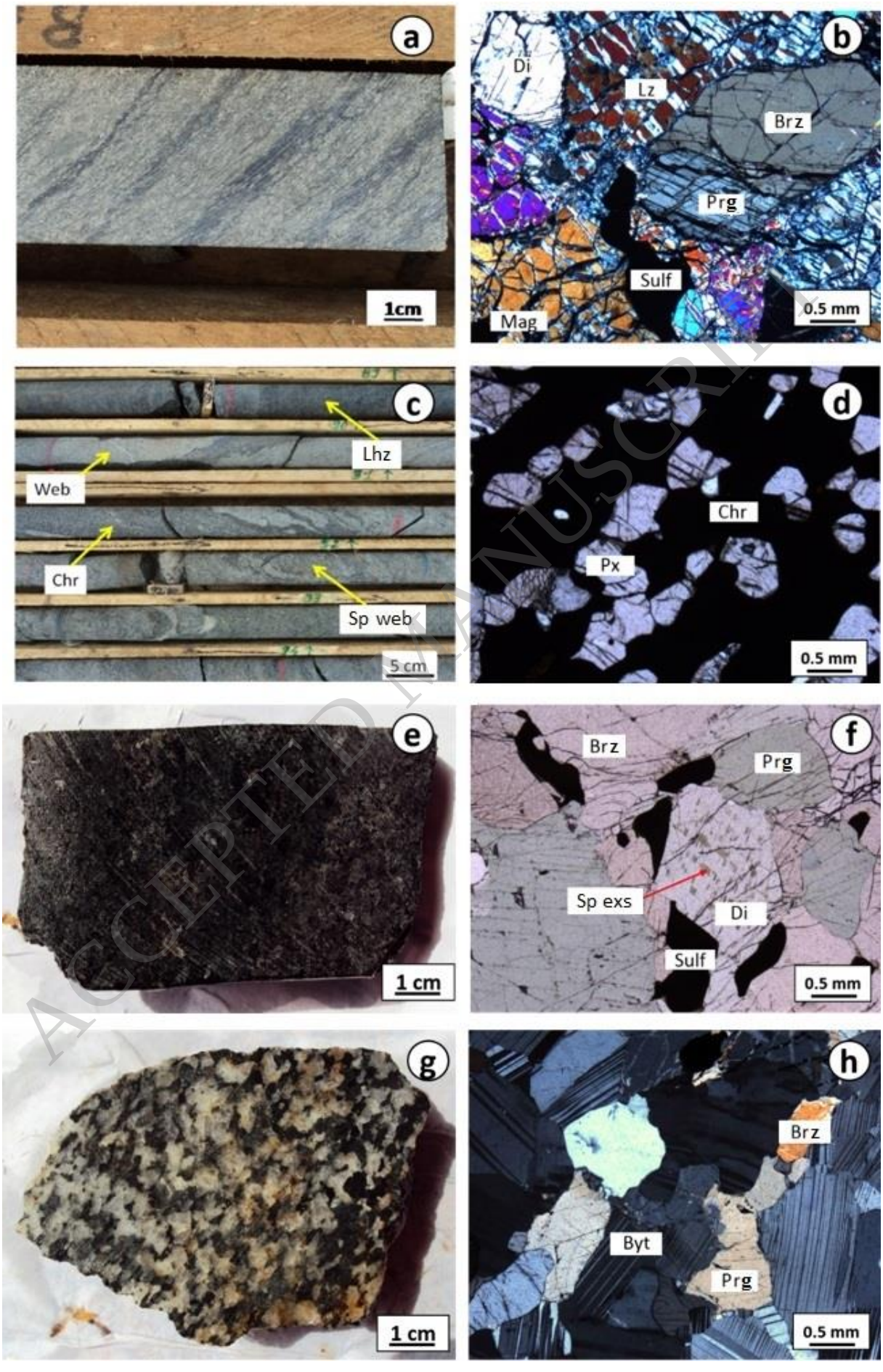

Fig. 3.

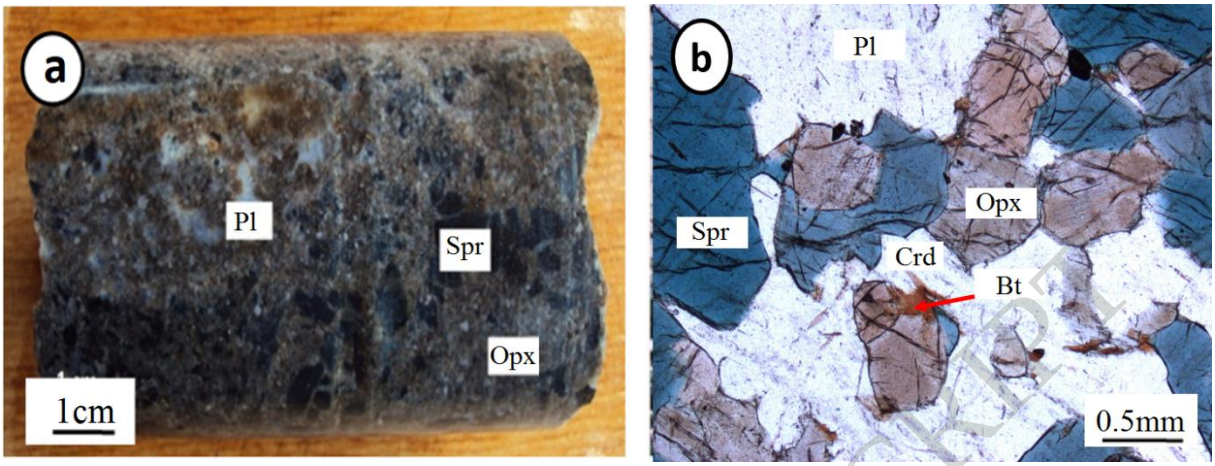

Fig. 4.

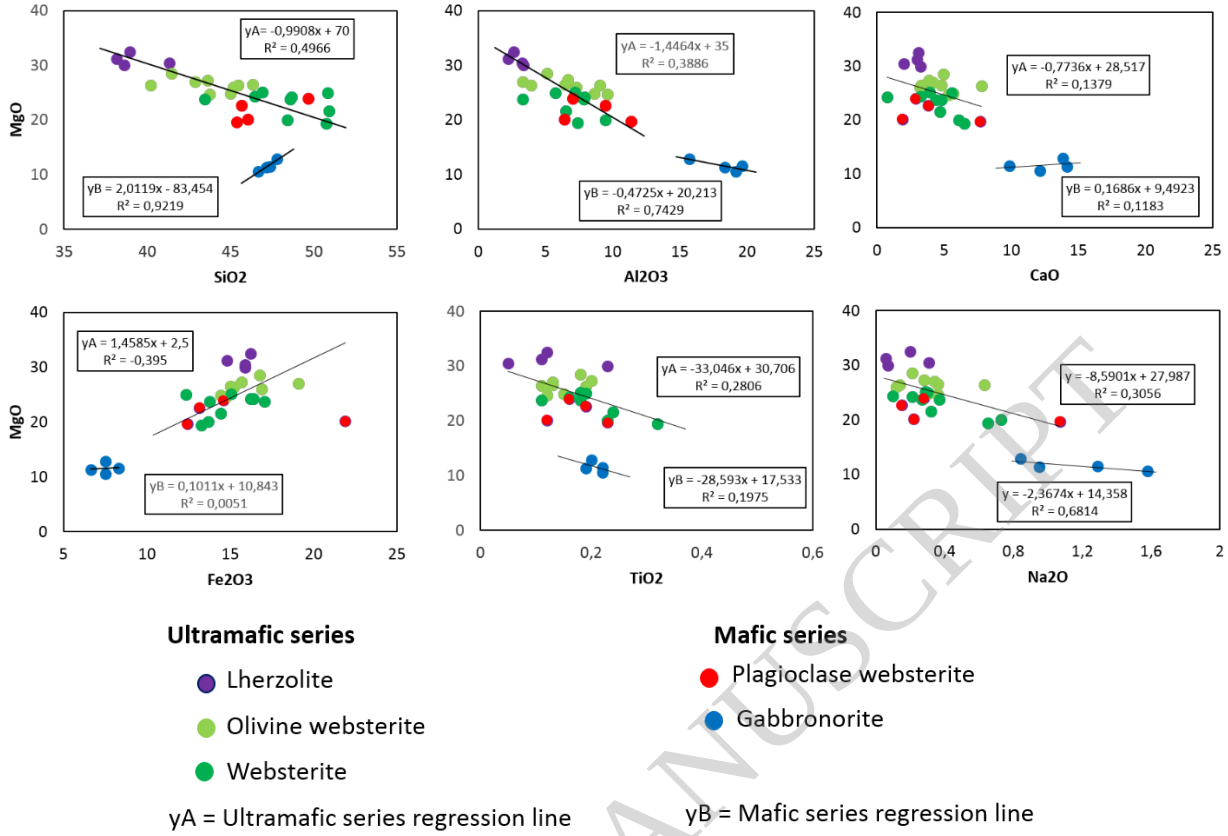

Fig. 5.

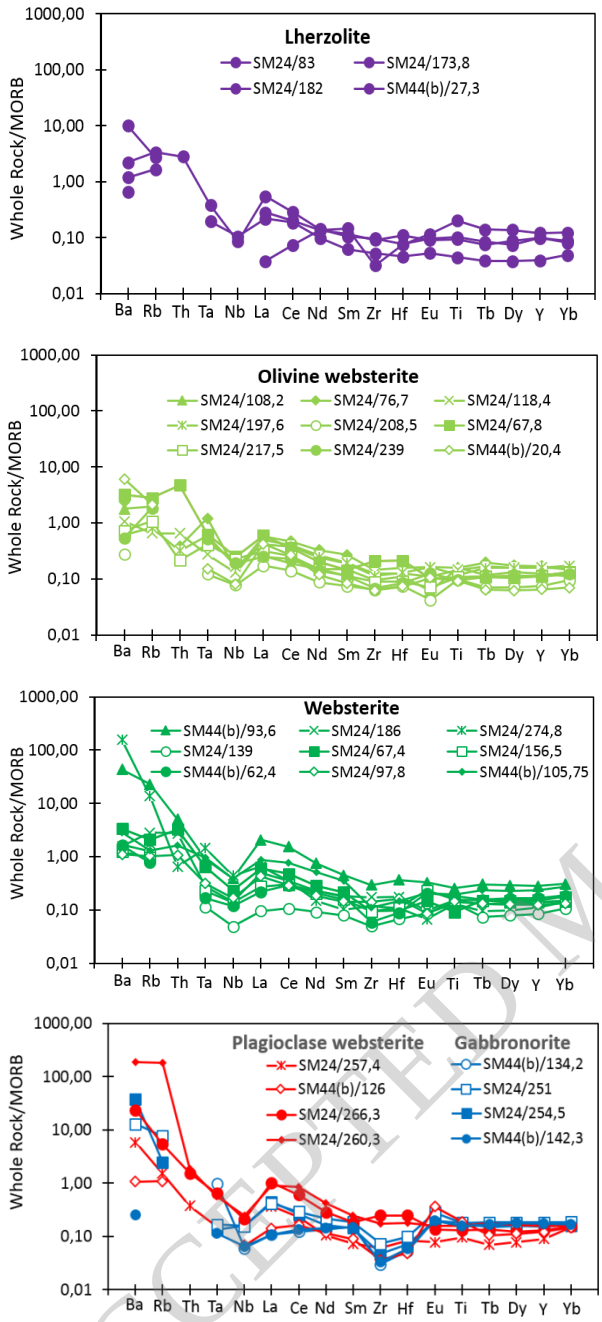

Fig. 6.

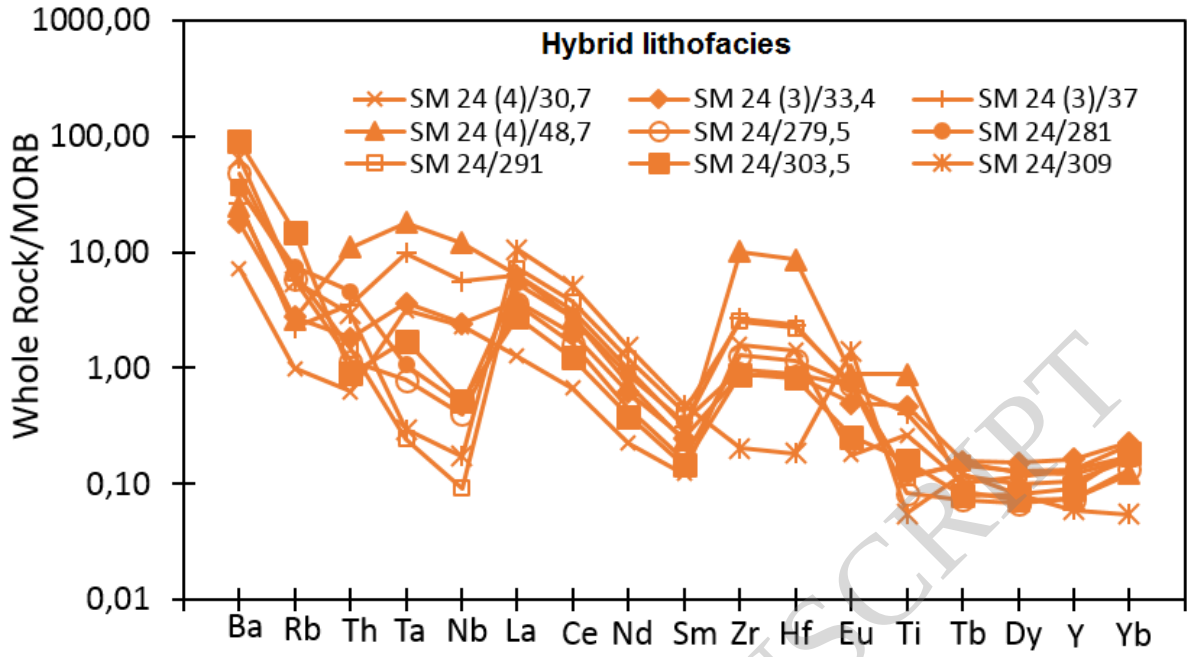

Fig. 7.

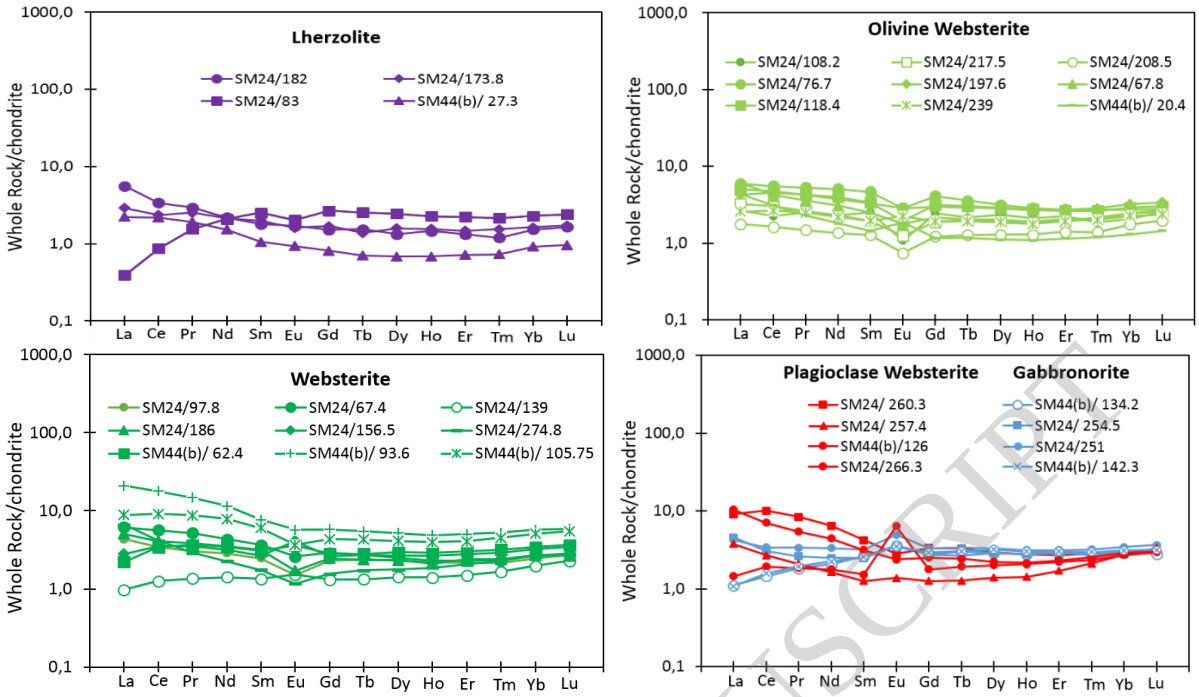

Fig. 8

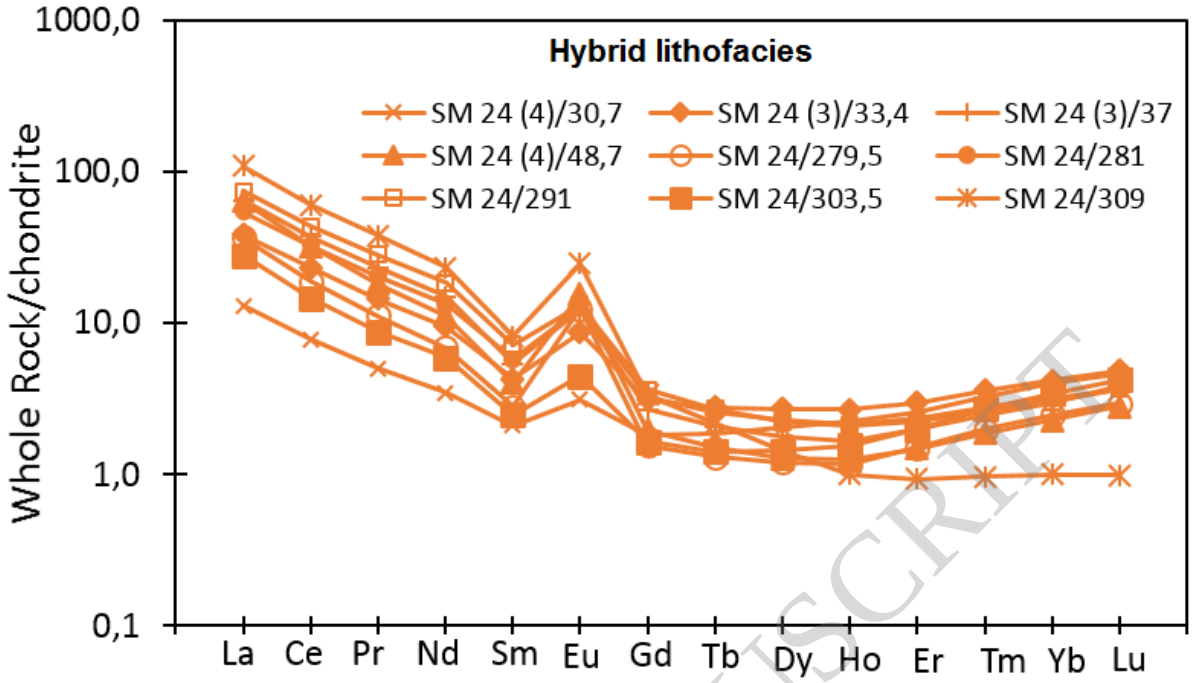

Fig. 9.

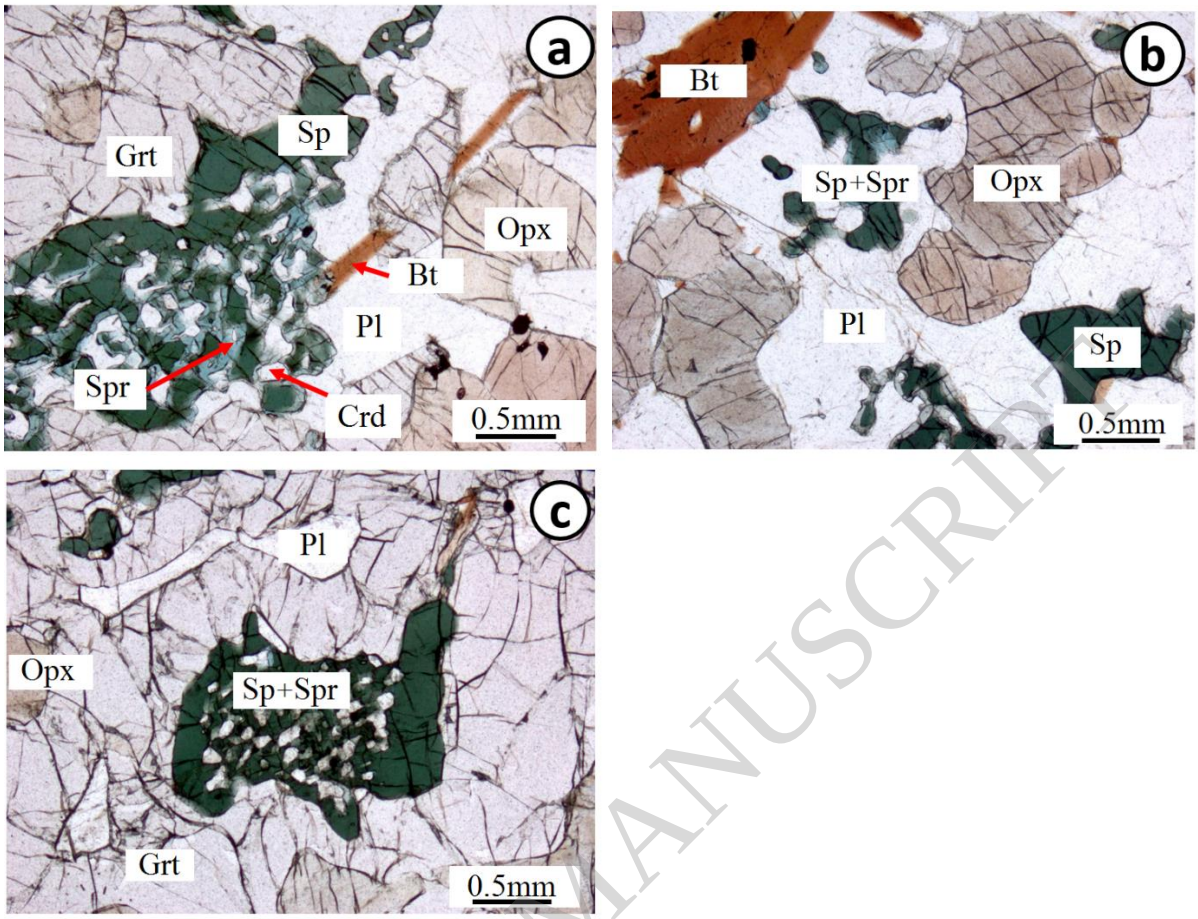

Fig. 10.

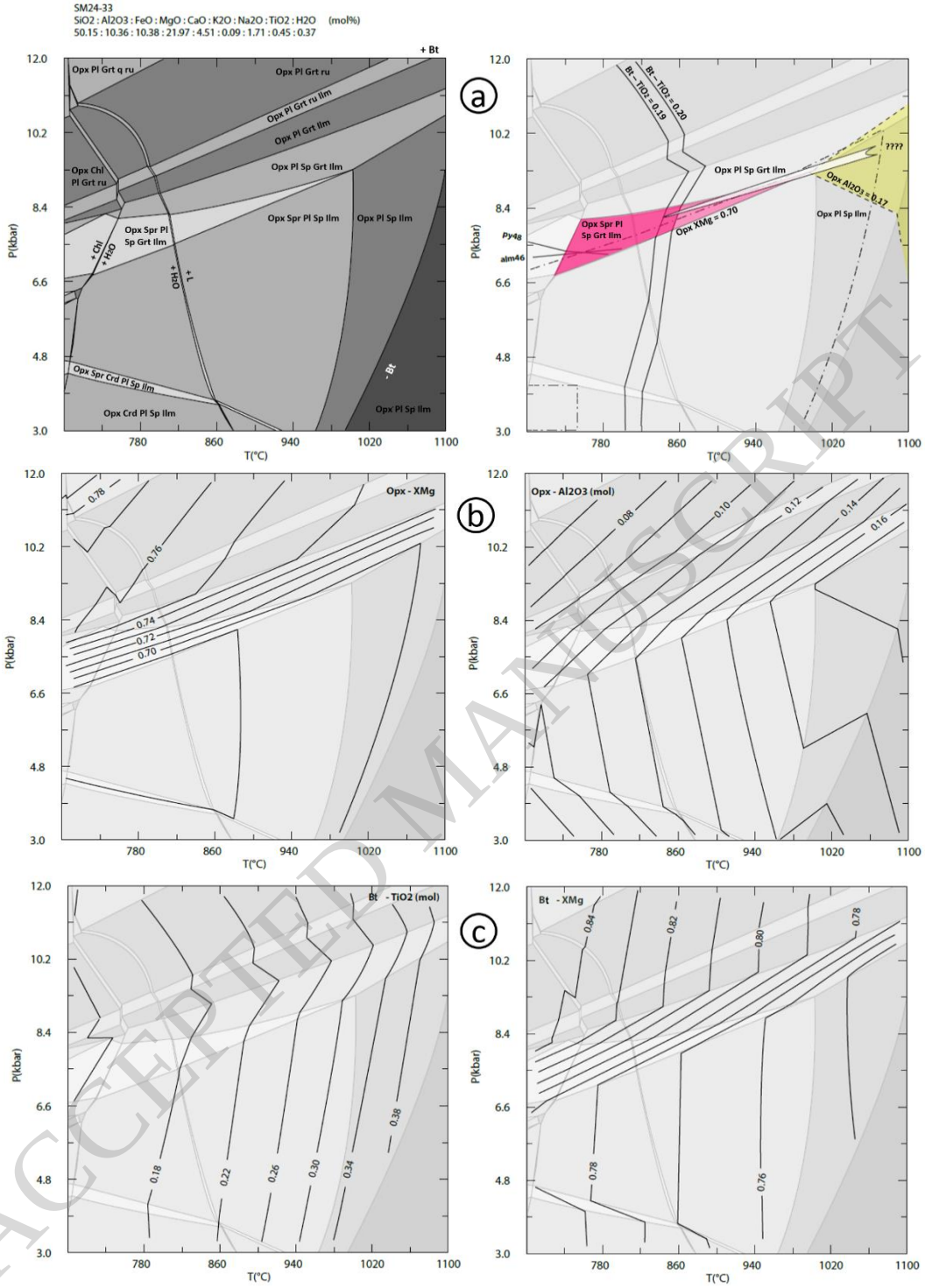

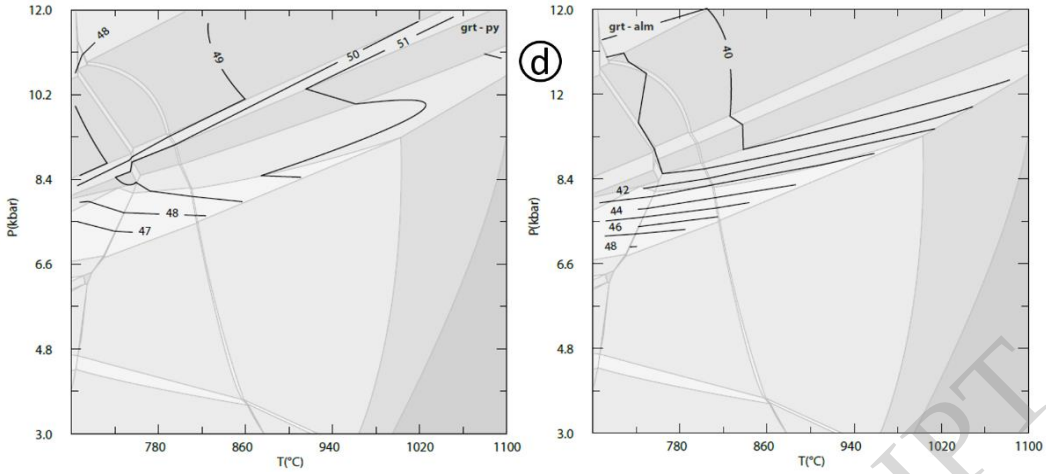

Fig. 11.

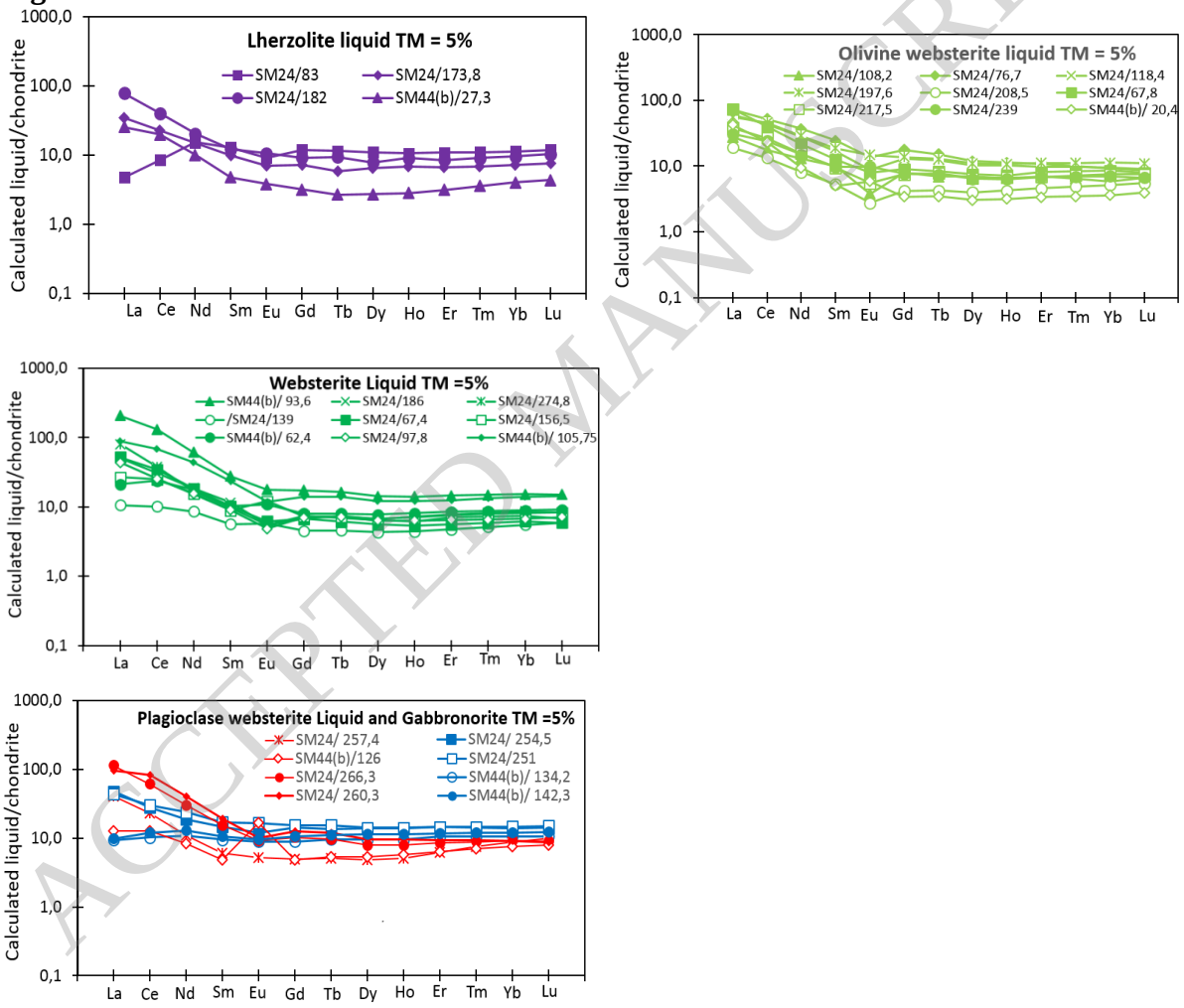

Fig. 12.

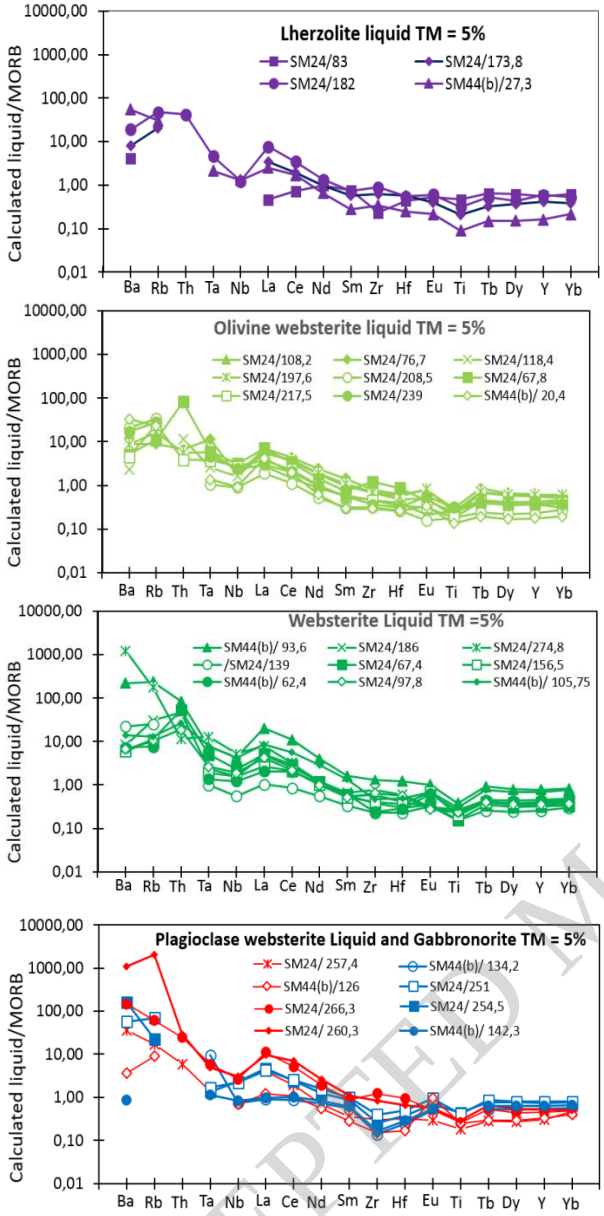

Fig. 13.

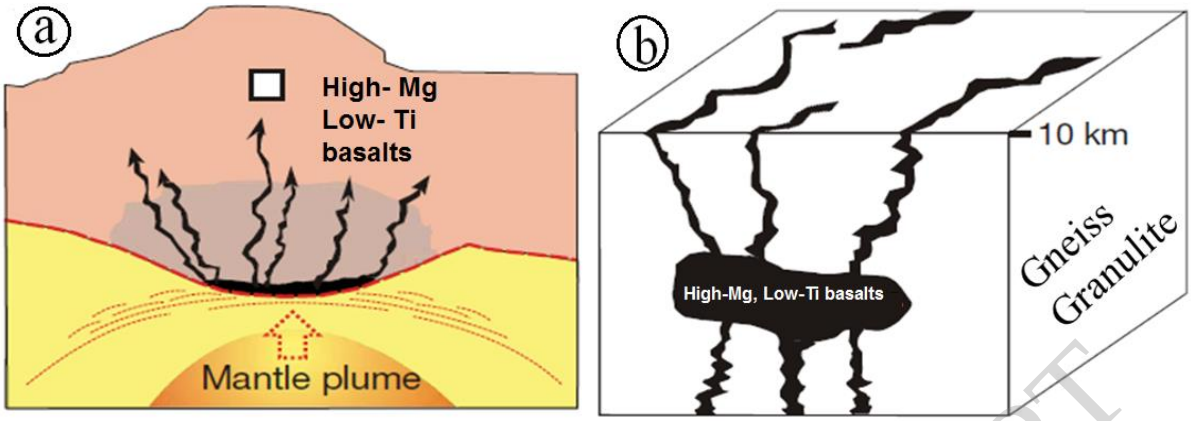

Fig. 14.